

## RESEARCH ARTICLE

10.1002/2017JD027460

## Secondary Gravity Waves in the Winter Mesosphere: Results From a High-Resolution Global Circulation Model

## Key Points:

- Primary and secondary GWs are resolved in the SH during winter using a new high-resolution GCM from the surface to the lower thermosphere
- Secondary GWs are created by localized and intermittent body forces from the dissipation of mountain waves near the stratopause
- Significant eastward drag and an eastward wind peak are created in the polar mesopause region by the dissipation of secondary GWs

## Correspondence to:

E. Becker,  
becker@iap-kborn.de

## Citation:

Becker, E., & Vadas, S. L. (2018). Secondary gravity waves in the winter mesosphere: Results from a high-resolution global circulation model. *Journal of Geophysical Research: Atmospheres*, 123. <https://doi.org/10.1002/2017JD027460>

Received 17 JUL 2017

Accepted 26 DEC 2017

Accepted article online 10 FEB 2018

Erich Becker<sup>1</sup>  and Sharon L. Vadas<sup>2</sup> <sup>1</sup>Leibniz Institute of Atmospheric Physics, Kühlungsborn, Germany, <sup>2</sup>Northwest Research Associates, Boulder, CO, USA

**Abstract** This study analyzes a new high-resolution general circulation model with regard to secondary gravity waves in the mesosphere during austral winter. The model resolves gravity waves down to horizontal and vertical wavelengths of 165 and 1.5 km, respectively. The resolved mean wave drag agrees well with that from a conventional model with parameterized gravity waves up to the midmesosphere in winter and up to the upper mesosphere in summer. About half of the zonal-mean vertical flux of westward momentum in the southern winter stratosphere is due to orographic gravity waves. The high intermittency of the primary orographic gravity waves gives rise to secondary waves that result in a substantial eastward drag in the winter mesopause region. This induces an additional eastward maximum of the mean zonal wind at  $z \sim 100$  km. Radar and lidar measurements at polar latitudes and results from other high-resolution global models are consistent with this finding. Hence, secondary gravity waves may play a significant role in the general circulation of the winter mesopause region.

**Plain Language Summary** We present a new gravity-resolving general circulation model that extends into the lower thermosphere. The simulated summer-to-winter-pole circulation in the upper mesosphere is nearly realistic and driven by resolved waves. We find a new phenomenon that results from the generation of secondary gravity waves in the stratosphere and lower mesosphere. The effect is characterized by an eastward gravity drag that causes a secondary eastward wind maximum around the polar winter mesopause. Analysis of the simulated gravity waves shows consistence with other gravity wave resolving models and with observational studies of the austral winter middle atmosphere, including the mesopause region.

## 1. Introduction

The general circulation of the middle atmosphere is dynamically controlled by waves generated in the troposphere. In the extratropics, quasi-stationary planetary Rossby waves and orographically generated mesoscale gravity waves (GWs) generate the relevant wave drag that drives the residual circulation during the winter up to the stratopause region (Alexander et al., 2010), while nonorographic GWs with horizontal phase speeds of tens  $\text{m s}^{-1}$  control the summer-to-winter-pole circulation in the mesopause region (Lindzen, 1981). In the mesosphere and lower thermosphere (MLT), this picture is further complicated by traveling planetary waves that develop as a result of baroclinic instability maintained by the GW-driven circulation (McLandress et al., 2006; Sato & Nomoto, 2015) and by the influence of thermal tides (Becker, 2017, hereafter, B17).

The GW activity in the middle atmosphere includes the breakdown of GWs from the troposphere (so-called “primary” GWs) which gives rise to temporally and spatially localized momentum and energy fluxes (Fritts et al., 2002, 2006; Smith et al., 2016). The intermittency of the associated strong body forces and related imbalances can create upward and downward propagating “secondary” GWs (Vadas & Fritts, 2002; Vadas et al., 2003). These secondary GWs have downward intrinsic phase propagation above and upward intrinsic phase propagation below the generation altitude. If the body forces have no temporal variability, no secondary GWs are excited (Vadas & Fritts, 2001). The secondary GW spectrum spans a large range of horizontal wavelengths  $\lambda_H$  and peaks at  $\lambda_H \sim 2L$ , where  $L$  is the full width of the body force. Secondary GWs are also generated by strong nonlinearities that occur when the primary waves break; these secondary GWs are generated at “higher harmonics” and typically have shorter scales and higher frequencies than the primary GWs (Bacmeister & Schoeberl, 1989; Satomura & Sato, 1999; Franke & Robinson, 1999).

Because secondary GWs from the former mechanism have larger horizontal and vertical scales, larger phase speeds, and smaller amplitudes than the primary GWs, they can propagate significant distances vertically before breaking or dissipating. This allows for the transfer of momentum and energy to higher altitudes. In particular, upward propagating secondary GWs with significant initial amplitudes can break and generate additional body forces several scale heights above the region of their generation.

The mechanism by which secondary GWs are generated from the deposition of momentum that occurs when primary GWs dissipate was first investigated in detail in the thermosphere. Model simulations show that primary GWs excited by deep convection can propagate well into the thermosphere, where they break or dissipate (Vadas & Liu, 2009, 2013; Vadas & Crowley, 2010). This process creates intermittent, localized body forces which excite secondary GWs having  $\lambda_H \sim 100\text{--}1,000$  s km (Vadas & Crowley, 2010); these secondary GWs then propagate to much higher altitudes and create significant variability in the neutral wind (Vadas & Crowley, 2017). Additionally, these secondary GWs enhance the variability of the ionosphere by creating medium to large-scale traveling ionospheric disturbances via ion drag (Azeem et al., 2017; Nicolls et al., 2014; Vadas & Crowley, 2017; Vadas & Nicolls, 2009).

Recent observational evidence suggests that secondary GWs may be generated in the austral winter polar stratosphere and observed in the MLT, because the GWs in the MLT have different characteristics than the GWs in the stratosphere and because a significant fraction of the GWs from  $z \sim 30\text{--}50$  km show upward phases in time (Chen et al., 2013, 2016; Yamashita et al., 2009; Zhao et al., 2017). Although many of the persistent large-amplitude GWs measured by lidar in the mesopause region during austral winter might have been secondary GWs generated in the stratosphere, it is not possible to determine from those observations which of the MLT GWs are primary or secondary GWs. Additionally, GW momentum flux (MF) estimates based on meteor radar measurements east of the Southern Andes reveal a significant vertical flux of eastward momentum (de Wit et al., 2017). This finding cannot be explained by nonorographic tropospheric GWs with eastward phase speeds because such waves are subject to critical level filtering by the strong polar vortex in the stratosphere and lower mesosphere. de Wit et al. (2017) argued that the eastward fluxes were secondary GWs excited in the stratosphere from mountain wave breaking over the Southern Andes.

Although these observations suggest that secondary GWs might be responsible for some of the variability in the polar winter MLT, no modeling study has investigated this mechanism in detail nor has examined the possible effects of secondary GWs on the general circulation of the middle atmosphere. The purpose of this model study is to investigate if and to what extent secondary GWs affect the general circulation of the MLT. We focus on winter in the southern hemisphere (SH) because the mean wintertime GW drag in the SH is much stronger than in the northern hemisphere (NH) (Geller et al., 2013). Accordingly, we expect the primary GW packets to result in stronger intermittent body forces and/or higher nonlinearities in the region of the maximum westward GW drag, that is, in the stratosphere and lower mesosphere at middle and polar latitudes during wintertime.

To simulate secondary GWs, we employ a general circulation model (GCM) with a high spatial resolution that describes GWs and their nonlinear interactions explicitly. Our GCM is the recently improved Kühlungsborn Mechanistic GCM (hereafter, KMCM). A former high-resolution version of the KMCM was used, for example, in Becker (2009) (hereafter, B09), Becker and von Savigny (2010), and Becker and Brune (2014). No GW parameterization is used in the high-resolution KMCM. However, we still parameterize unresolved macroturbulence in terms of horizontal and vertical diffusion. To date, this model concept is employed in only two other GCMs that extend into the lower thermosphere and simulate semirealistic GW effects in the mesopause region: The JAGUAR model (Watanabe & Miyahara, 2009) which is a vertical extension of the KANTO model (e.g., Sato et al., 2012; Watanabe et al., 2008), and a high-resolution version of the Whole Atmosphere Community Climate Model (Liu et al., 2014). The tropospheric sources of the resolved GWs in a GCM are due to imbalances induced by large amplitudes or breakdown of baroclinic Rossby waves (O'Sullivan & Dunkerton, 1995; Plougonven & Zhang, 2014), imbalances resulting from parameterized convection (Liu et al., 2014), and flow over steep terrain (Sato et al., 2012). In the current study we focus on the importance of orographically generated GWs in the SH, the corresponding westward drag in the winter stratosphere and lower mesosphere, the excitation of secondary GWs, and the additional eastward drag in the MLT from the dissipation of these secondary GWs.

The organization of our paper is as follows. In section 2 we provide a brief model description. Section 3 presents our GW diagnostics and the zonal-mean climatology for austral winter. In section 4 we analyze the geographical and temporal variability of the resolved GWs. Our conclusions are contained in section 5.

## 2. Model Description

The KMCM is based on a standard spectral dynamical core with a terrain-following vertical coordinate and a staggered vertical grid according to Simmons and Burridge (1981). We employ a triangular spectral truncation at total horizontal wave number 240 and 190 full model layers (T240L190). The spectral truncation corresponds to a grid spacing of  $\sim 55$  km, and the shortest resolved horizontal wavelength is  $\lambda_H \sim 165$  km. The vertical level spacing is  $\sim 600$  m between the boundary layer and  $3 \times 10^{-4}$  hPa ( $z \sim 100$  km). The level spacing increases in the lower thermosphere, and the highest model layer is located at  $1.5 \times 10^{-5}$  hPa ( $z \sim 135$  km).

The new version of the KMCM includes simplified but nevertheless explicit representations of the relevant components of a climate model: radiative transfer, water vapor transport and convection, and the full surface energy budget which includes a slab ocean. These methods were described in more detail in Becker et al. (2015) where the KMCM was used with “conventional resolution” and with GW parameterizations (see also B17). Here conventional resolution refers to a T32L70 model which resolves waves with  $\lambda_H \geq 1,250$  km and has a level spacing of  $\sim 2$  km in the MLT.

The new KMCM with T240L190 resolution does not include GW parameterization. The subgrid-scale (macro)turbulent diffusion scheme is essentially the same as in B09. In particular, the Smagorinsky scheme (Becker & Burkhardt, 2007; Smagorinsky, 1993) is used for both horizontal and vertical diffusion. B09 found that it is crucial that both diffusion coefficients depend on the local Richardson number in order to damp GWs by anisotropic diffusion when they become dynamically unstable. This is different from other models where the effects of horizontal diffusion are imposed by prescribed linear damping in terms of hyperdiffusion, numerical filtering, or Rayleigh friction. The current high-resolution version of the KMCM also includes an additional hyperdiffusion, but this affects only total wave numbers larger than 210 and ensures a realistic cutoff of the global kinetic energy spectrum (Becker & Brune, 2014; Brune & Becker, 2013). In order to damp waves propagating into the lower thermosphere, an additional linear (harmonic) diffusion is applied above  $\sim 110$  km (i.e., a “sponge” layer). The model thermosphere includes a parameterization of ion drag (Hong & Lindzen, 1976). The molecular viscosity and diffusion, as well as the height dependencies of the heat capacity and the gas constant, are given by Vadas (2007). We emphasize that all parameterizations of subgrid-scale processes in the KMCM fulfill the energy conservation law. In particular, the complete frictional heating due to momentum diffusion and ion drag is included. The importance of this constraint for simulating the MLT was demonstrated in B17. Furthermore, all subgrid-scale terms, except ion drag, preserve angular momentum.

The model was integrated with a conventional spectral resolution until an equilibrated climatology was reached. We then increased the spectral resolution to T240, adjusted the diffusion parameters, and integrated one model year starting in April. For convenience, a model year has 360 days and each month has 30 days. Snapshots were archived every 22.5 min.

A T240 spectral resolution can represent well many details of the terrestrial topography (see Figure 1a). For example, the topography of islands such as Iceland, Hawaii, and New Zealand are all represented with this resolution and appear in Figure 1a. The surface heat capacity applied in the KMCM (Figure 1b) reflects these details. We apply a 10 times smaller heat capacity for land surfaces than for ocean surfaces. A reduced oceanic heat capacity is applied in the tropics since here the mixed layer is less deep than at middle latitudes. We generally apply the land value for surface heat capacity at northern polar latitudes in order to represent ice surfaces. Land-sea masks are also applied for the surface albedo, as well as for the roughness length and the relative humidity at the surface that are used in the boundary layer scheme (not shown).

Figures 1c and 1d show a typical daily average during austral winter of the vertically integrated latent plus sensible heating and the corresponding surface flux of latent plus sensible heat. These fields are dominated by the latent heating (precipitation) and the surface evaporation. The two patterns are quite distinct, although their global integrals are nearly identical in the climatological mean and roughly comparable on a daily mean basis. Comparing Figures 1c and 1d demonstrates that the KMCM simulates the convergence of the latent heat flux in the tropical convergence zone and at middle latitudes, whereas the evaporation occurs mainly in the subtropics and at middle latitudes over water surfaces. Furthermore, the latent heating in the extratropics is concentrated along the fronts of the resolved weather systems (i.e., the baroclinic Rossby waves). These features confirm that the new KMCM with an explicit moisture cycle simulates realistic large-scale tropospheric dynamics like the model version of B09. We therefore expect that the extratropical nonorographic GW sources are also comparable with those in the former model version.

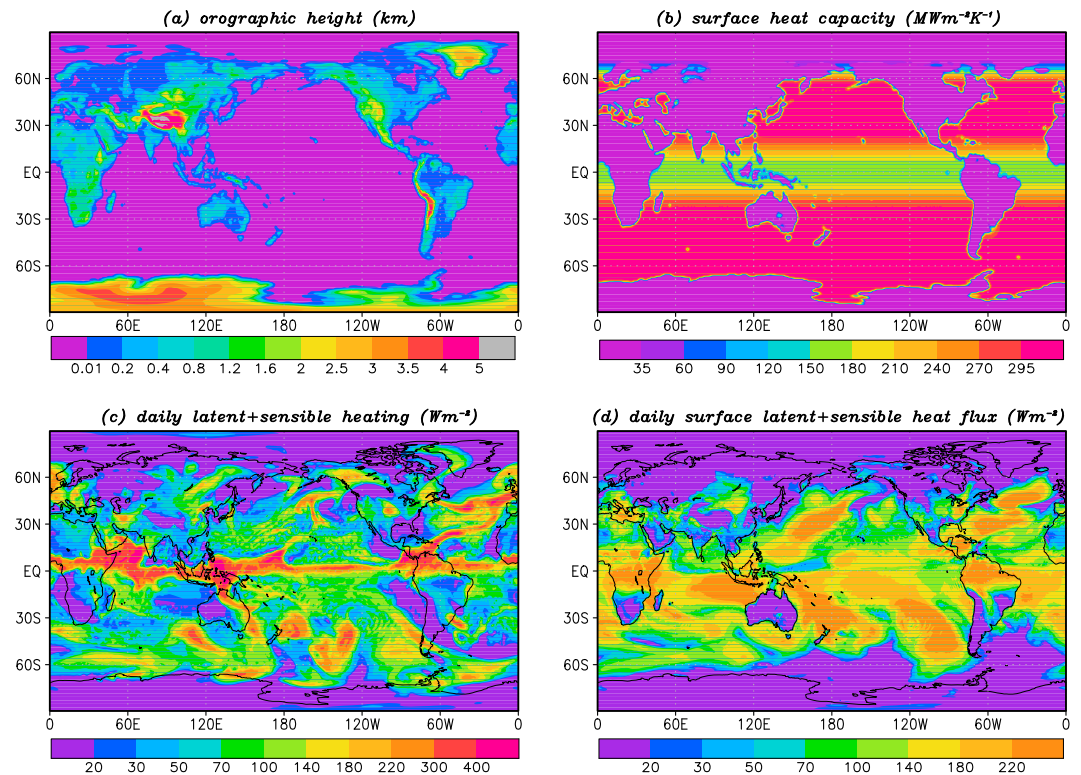


**Figure 1.** Surface parameters and simulated moisture cycle. (a) Orographic height (km). (b) Surface heat capacity ( $10^6 \text{ W m}^{-2} \text{ K}^{-1}$ ). (c) Daily averaged and vertically integrated latent plus sensible heating for 1 July of the simulation. (d) Surface latent plus sensible heat flux averaged for 1 July. The unit in (c) and (d) is  $\text{W m}^{-2}$ .

Alexander et al. (2016) and Sato et al. (2012) showed with the KANTO model that the orography represented even with a T213 resolution simulates orographic GW fluxes that provide reasonable drag in the middle atmosphere. In particular, these studies confirmed that the resolved orographic GWs propagate downstream from their source region and have considerable intermittency as compared to the resolved nonorographic GWs. Since the resolution and dynamical core of the KMCM is similar to that of the KANTO model, we also expect the KMCM to resolve the effects of orographic GWs in the middle atmosphere.

### 3. Zonal-Mean Flow and GW Diagnostics

Figure 2 shows the simulated zonal-mean climatology averaged from 21 June to 10 August. The zonal wind and temperature ( $[u]$  and  $[T]$ , colors in Figure 2) are quite reasonable and compare well with results of Watanabe and Miyahara (2009) for July. The sum of the Eliassen-Palm flux (EPF) divergence and ion drag ( $\text{Div}(\text{EPF}) + \text{ID}$ ) and the residual mass stream function ( $\Psi_{\text{res}}$ ) are shown with black contours in Figure 2. The ion drag is negligible below  $10^{-4}$  hPa ( $\sim 110$  km). The resolved waves drive a summer-to-winter-pole circulation in the mesosphere that is comparable to the circulation produced by models with GW parameterization. The EPF divergence is negative (westward) in the winter MLT but exceeds  $+20 \text{ m s}^{-1} \text{ d}^{-1}$  in the region marked grey around  $70^\circ\text{S}$  and  $10^{-4}$  hPa in Figure 2b.

The westward maximum of the EPF divergence around  $55^\circ\text{S}$  and from about 0.3 to 0.003 hPa ( $\sim 55$  to 85 km) is dominated by the resolved GWs (see also Figure 3e below). This westward maximum includes the contribution from eastward traveling planetary waves. Eastward traveling waves have been observed during winter from the stratosphere to the lower thermosphere (e.g., Garcia et al., 2005; Lu et al., 2013). In our model simulation, these waves exert a positive (eastward) EPF divergence of about  $20\text{--}30 \text{ m s}^{-1} \text{ d}^{-1}$  centered around  $65^\circ\text{S}$  and reaching from about 0.1 to 0.01 hPa ( $\sim 60$  to 80 km, not shown).

Poleward circulation branches can be seen in the lower thermosphere. As shown in B17, these are caused by the predominantly westward EPF divergence due to thermal tides, although this effect is somewhat stronger here. Note that although the sponge layer forces the tides (and other resolved waves) to deposit their

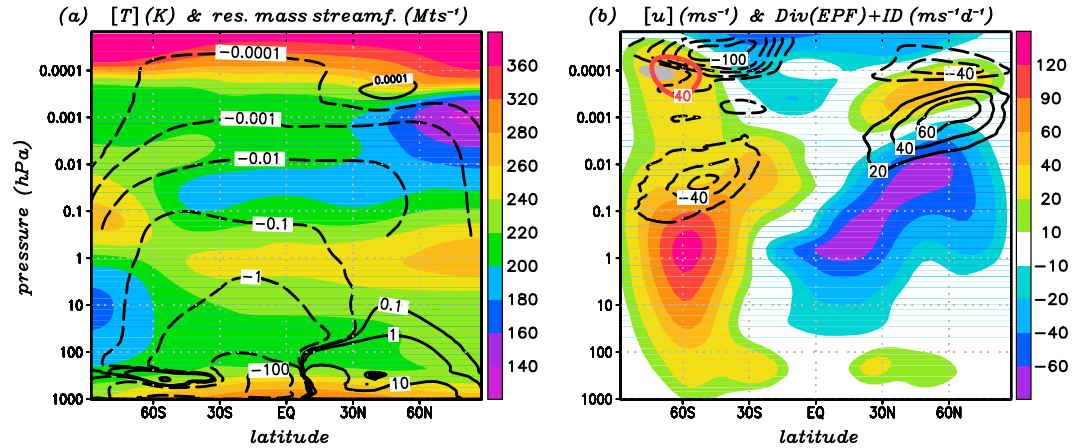


**Figure 2.** Zonal-mean model climatology during austral winter (21 June to 10 August). (a) Temperature (colors) and residual mass stream function (contours for  $\pm 0.0001, -0.001, -0.01 \times 10^9 \text{ kg s}^{-1}$  above 0.3 hPa and for  $\pm 0.1, \pm 1, \pm 10$ , and  $-100 \times 10^9 \text{ kg s}^{-1}$  farther below). (b) Zonal wind (colors) and the sum of the Eliassen-Palm flux (EPF) divergence and ion drag (Div(EPF)+ID, contours for  $\pm 20, \pm 40, \pm 60, -80$ , and  $-100 \text{ m s}^{-1} \text{ d}^{-1}$ ). The red  $40 \text{ m s}^{-1}$  contour marks the additional wind maximum in the southern mesopause region. The grey shading in the same region marks values of Div(EPF)+ID exceeding  $+20 \text{ m s}^{-1} \text{ d}^{-1}$ . The vertical coordinate is the vertical hybrid coordinate of the model times 1,013 hPa, it extends from the surface to about 135 km.

momentum and energy in the upper model domain, the particular sponge layer used in the KMCM ensures that no spurious angular momentum or energy is added to the flow (see also the discussion in B17).

The additional eastward wind maximum around  $60^\circ\text{S}$  and  $3 \times 10^{-4} \text{ hPa}$  ( $z \sim 100 \text{ km}$ , marked by the red contour in Figure 2b) is also seen in Figure 1c of Watanabe and Miyahara (2009). However, Watanabe and Miyahara (2009) assumed that this feature was an artifact of the applied hyperdiffusion, and no further explanation was given. Because the JAGUAR model is also a high-resolution GW-resolving model, it is likely that the additional wind maximum simulated here in the KMCM was also simulated in the JAGUAR model for the same reason. The same feature is also simulated with the high-resolution version of the Whole Atmosphere Community Climate Model for austral winter conditions (Hanli Liu, 2017, private communication), although this feature was not mentioned in Liu et al. (2014). We therefore argue that the additional eastward wind maximum at  $z \sim 100 \text{ km}$  is a robust feature of GW-resolving GCMs which extend into the thermosphere. We shall show below that this feature is caused by the momentum deposition of eastward propagating secondary GWs that are generated in the stratopause region from the drag accompanying the dissipation of primary GWs.

In order to analyze the simulated GWs in more detail we exploit the spectral expansion of the prognostic variables into spherical harmonics. B09 found that even for a T120 spectral resolution, the GW momentum deposition and the dissipative heating of resolved GWs are due to horizontal wavelengths shorter than 1,000 km. Note that the GW energy density will generally maximize at scales larger than the scales responsible for the GW drag. Since we focus on GW-mean flow effects rather than on the GW perturbations in temperature and winds, we assume a scale separation similar to that used in B09. More specifically, we reconstruct all flow variables from our simulation using triangular spectral truncations of T30, T100, T200, and T240. Using the indices T30, T100, T200, and T240 for the different spectral truncations, we define the mean flow variables as  $X_{T30}$ , where  $X$  represents temperature, density, geopotential, or wind components. Total GW variables are defined using  $X' = X_{T240} - X_{T30}$ . Large-scale, medium-scale, and small-scale GW variables are defined as  $X^l = X_{T100} - X_{T30}$ ,  $X^m = X_{T200} - X_{T100}$ , and  $X^s = X_{T240} - X_{T200}$ , respectively. These GW scales correspond to horizontal wavelengths  $\lambda_h$  from  $\sim 1,350 \text{ km}$  down to 400 km (large-scale GWs), from about 400 km down to 200 km (medium-scale GWs), and from about 200 down to 165 km (small-scale GWs). Horizontal averages over areas of about  $1,350 \times 1,350 \text{ km}^2$  will be denoted by a bar. We use the abbreviation  $\bar{X} = \bar{X}_{T30}$  for area-averaged mean flow variables.

Using pressure  $p$  as the vertical coordinate, the related GW fluxes of momentum and potential energy per unit mass are computed according to (see also B17 and Shaw and Becker, 2011):

$$(F_u^\delta, F_v^\delta) = -(g\bar{\rho})^{-1} (\overline{u^\delta \omega^\delta}, \overline{v^\delta \omega^\delta}) \quad (1)$$

$$F_p^\delta = -(g\bar{\rho})^{-1} \overline{\Phi^\delta \omega^\delta}, \quad (2)$$

respectively, where the upper index  $\delta$  represents either  $\ell$ ,  $m$ , or  $s$  for the three spectral compartments of the resolved mesoscales. Furthermore,  $\mathbf{v} = (u, v)$  and  $\omega$  are the horizontal wind vector and the total time derivative of  $p$ , respectively,  $\rho$  is density,  $\Phi$  is geopotential, and  $g$  is gravitational acceleration. The total GW fluxes and drag components per unit mass are defined as

$$(F_u, F_v) = -(g\bar{\rho})^{-1}(\overline{u'\omega'}, \overline{v'\omega'}) \approx (F_u^\ell, F_v^\ell) + (F_u^m, F_v^m) + (F_u^s, F_v^s) \quad (3)$$

$$F_p = -(g\bar{\rho})^{-1}\overline{\Phi'\omega'} \approx F_p^\ell + F_p^m + F_p^s \quad (4)$$

$$(\text{GWD}_u, \text{GWD}_v) = -\partial_p(\overline{u'\omega'}, \overline{v'\omega'}). \quad (5)$$

For comparison with other studies we also diagnose the so-called absolute GW momentum flux. The squared absolute momentum flux is defined as (e.g., Alexander et al., 2016, their equation (1)):

$$\text{MF}^2 = \bar{\rho}^2(\overline{\mathbf{v}'^2} \overline{w'^2})(1 - \alpha^2)^2(1 + \alpha^2), \quad \alpha^2 = \frac{f^2}{N^2} \frac{g^2 \overline{T'^2}}{N^2 \overline{T'^2} \overline{w'^2}}. \quad (6)$$

Here  $f$  is the Coriolis parameter and  $N$  is the buoyancy frequency. The GW-related vertical wind perturbation is computed as  $w' = -\omega'/(g\bar{\rho})$ . Equation (6) gives the squared pseudo momentum flux of a monochromatic inertia GW, where  $\alpha$  is  $f$  divided by the intrinsic frequency. The quantity MF is often applied to characterize observed or simulated GW fields which usually consist of a broad spectrum of waves.

The GW energy flux is the sum of the potential and kinetic energy flux (Hines & Reddy, 1967):

$$\bar{\rho}F_e = \bar{\rho}(F_p + \bar{u}F_u + \bar{v}F_v). \quad (7)$$

Note that  $\bar{\rho}F_e$  and  $\bar{\rho}(F_u, F_v)$  are constant with height for conservative GWs in steady state and in the single column approximation (Lindzen, 1973). The energy flux is positive for upward propagating nonorographic GWs. Orographic GWs in steady state are a special case in which the energy flux is zero because the downward kinetic energy flux and the upward potential energy flux cancel each other. This is seen from the second theorem of Eliassen and Palm (see Lindzen, 1990, his equation (8.14)) which yields  $F_p = (c - \bar{u})F_u$  and  $F_e = cF_u$  for a monochromatic GW propagating in  $x$  direction with ground-based phase speed  $c$ . Hence, conservative mountain waves in steady state and in the single column approximation fulfill  $F_p = -\bar{u}F_u - \bar{v}F_v$  and  $F_e = 0$ .

The energy deposition of GWs per unit mass, denoted by the symbol  $E$ , is given by the sum of the dissipation rates of kinetic and potential energy. For resolved GWs, the energy deposition can be computed as (see B17)

$$\begin{aligned} \epsilon_m = & (K_h |S_h|^2)_{T240} - (K_h |S_h|^2)_{T30} \\ & + ((K_z + \nu)(g\rho\partial_p \mathbf{v})^2)_{T240} - ((K_z + \nu)(g\rho\partial_p \mathbf{v})^2)_{T30} \\ & + (\mathbf{v} \cdot (\mathbf{D}\mathbf{v}))_{T240} - (\mathbf{v} \cdot (\mathbf{D}\mathbf{v}))_{T30} \end{aligned} \quad (8)$$

$$\bar{\epsilon}_{th} = R/\rho(\overline{T'\omega'}) \quad (9)$$

$$E = \bar{\epsilon}_m + \bar{\epsilon}_{th}. \quad (10)$$

Here  $K_z$  and  $\nu$  are the turbulent and molecular vertical viscosities, respectively, and  $S_h$  and  $K_h$  are the horizontal strain tensor and turbulent diffusion coefficient (see section 2c in B09). The tensor  $\mathbf{D}$  consists of the ion drag coefficients, and  $R$  is the gas constant.

Figures 3a, 3c, 3e, and 3g show zonal-mean results for the SH middle atmosphere as diagnosed from the T240L190 model run and averaged from 21 June to 10 August. As usual, zonal averaging is indicated by square brackets. For comparison, Figures 3b, 3d, 3f, and 3h show the corresponding KMCM results when using a conventional T32L80 resolution combined with GW parameterizations and diagnosing the GW-related quantities from these parameterizations. For this purpose we use the July climatology from the control simulation of B17. Comparing Figures 3a and 3b shows that the additional eastward wind maximum around 60°S and  $3 \times 10^{-4}$  hPa ( $z \sim 80$  km) is not simulated with the conventional model setup. This is typical also for community middle atmosphere climate models that employ GW parameterization (e.g., Fomichev et al., 2002; Smith, 2012). The GW fluxes and mean flow effects shown in Figures 3c–3h are similar in both model versions up to about  $\sim 0.01$  hPa ( $z \sim 80$  km). However, the vertical GW flux of westward momentum and the corresponding westward GW drag at polar latitudes in the lower mesosphere are much stronger in the model with GW parameterization (compare Figures 3e and 3f). This is consistent with the finding of Geller et al. (2013)

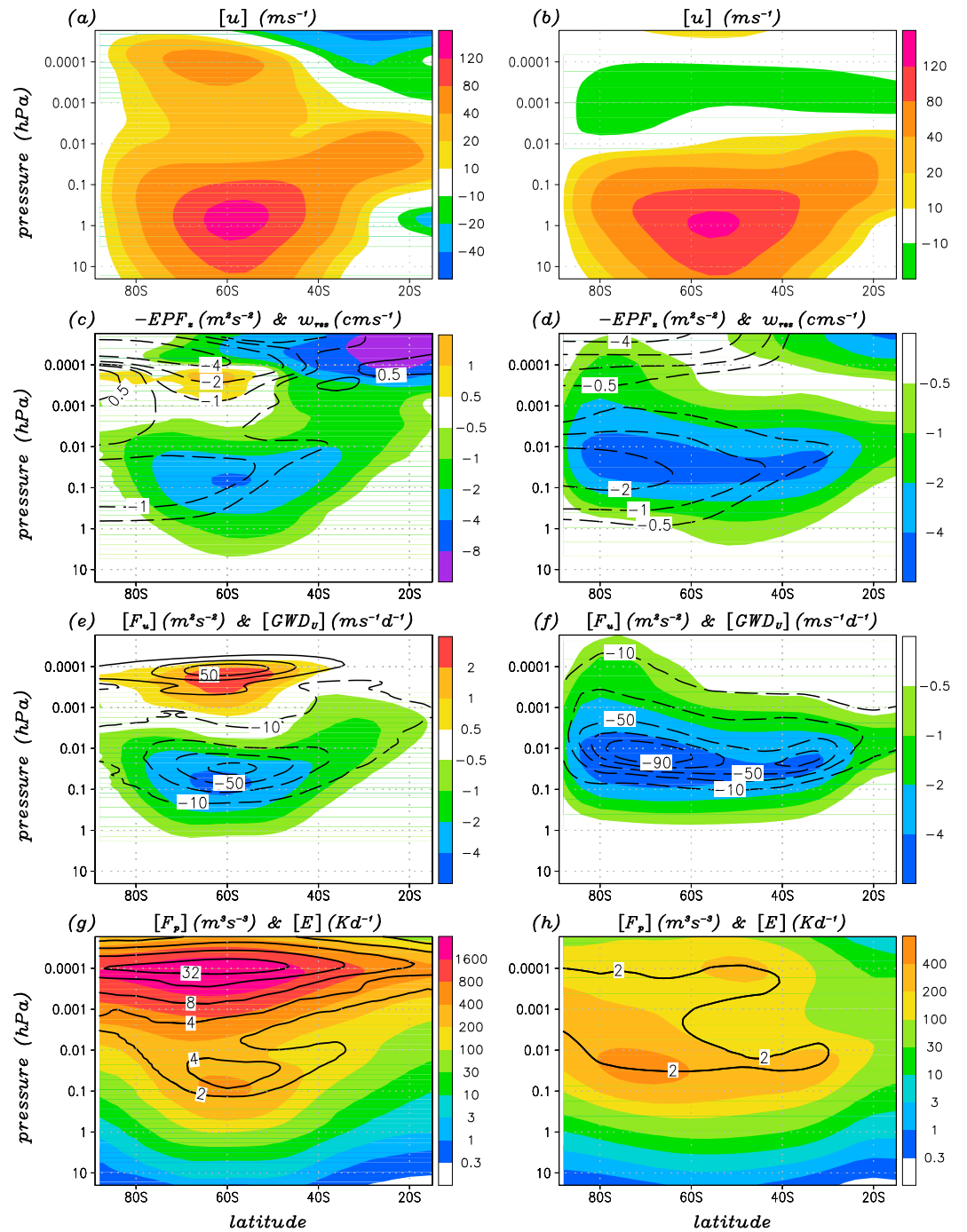


**Figure 3.** General circulation in the southern winter middle atmosphere: comparison of the T240L190 model with resolved gravity waves (GWs) (a, c, e, and g) against a corresponding T32L80 model version with parameterized GWs (b, d, f, and h). (a and b) Zonal-mean zonal wind. (c and d) Negative vertical component of the Eliassen-Palm flux ( $-EPF_z$ , colors, including the contribution from parameterized GWs in (d) and the residual vertical wind (contours for  $\pm 0.5, -1, -2, -4 \text{ cm s}^{-1}$ ). (e) Zonal-mean vertical momentum flux due to resolved GWs (colors) and the associated GW drag (contours for  $\pm 10, 30, 50, 70, 90 \text{ m s}^{-1} \text{ d}^{-1}$ ). (f) Same as (e) but for the parameterized GWs. (g) Zonal-mean potential energy flux (colors) and energy deposition (contours for 2, 4, 8, 16, 32  $\text{K d}^{-1}$ ) due to resolved GWs. (h) Same as (g) but for the parameterized GWs. The vertical axis extends from about 30 to 135 km.

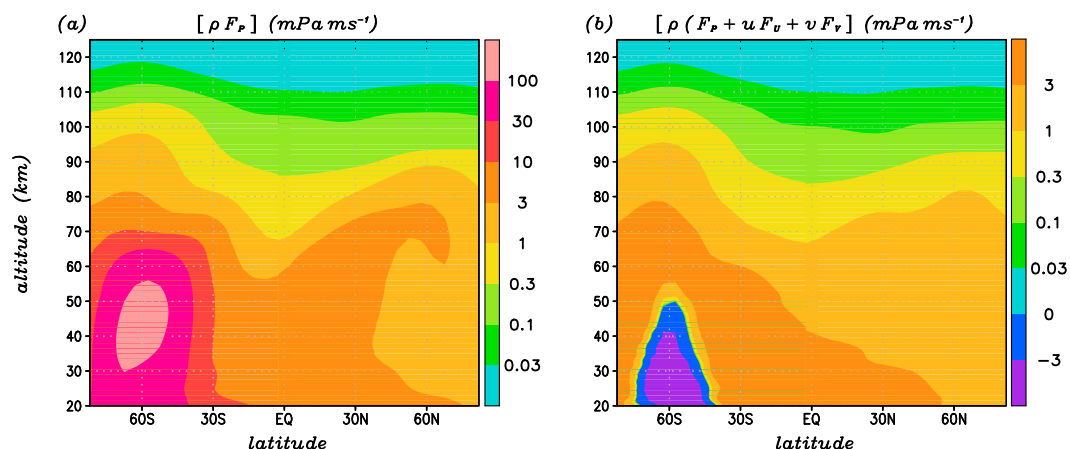


**Figure 4.** Zonal-mean potential and total (potential plus kinetic) energy flux density due to resolved gravity waves (averaged from 21 June to 10 August). For definitions see text and equations (3) and (4). The vertical coordinate is height above sea level.

that conventional models with GW parameterization overestimate the zonally averaged GW activity in the stratosphere and lower mesosphere close to the poles. This difference between the two model versions at high latitudes below 0.01 hPa ( $z \sim 80$  km) is also visible when we consider the complete vertical component of the negative EPF, denoted as  $-EPF_z$  (colors in Figures 3c and 3d), or the GW potential energy flux and the energy deposition due to GWs (Figures 3g and 3h).

The region above 0.01 hPa ( $z \sim 80$  km) in Figures 3c–3f exhibits qualitative differences between the two model versions. Whereas the vertical GW flux of westward momentum and  $-EPF_z$  extend well into the lower thermosphere poleward of  $60^\circ\text{S}$  in the conventional model (Figures 3d and 3f), there is a change in sign toward an upward flux of eastward momentum when GWs are resolved (Figures 3c and 3e). Another difference is seen at lower latitudes in the lower thermosphere, whereby  $-EPF_z$  is much stronger in the GW-resolving model. Here the EPF is dominated by thermal tides in both models. A closer inspection of the model data showed that the thermal tides are stronger in the T240L190 model. The differences in  $-EPF_z$  at middle and high latitudes are reflected by corresponding differences in the residual vertical wind (contours in Figures 3c and 3e). In particular, in the T240L90 model there is a region of upwelling close to the pole from  $10^{-3}$  to  $10^{-4}$  hPa ( $z \sim 90$ – $110$  km). This upwelling is related to a pronounced eastward GW drag centered around  $60^\circ\text{S}$  and  $3 \times 10^{-4}$  hPa ( $z \sim 100$  km). Both features are consistent with the additional wind maximum in the lower thermosphere in Figure 3a, as well as with a decrease of the temperature with latitude toward the South Pole in the height range from  $10^{-3}$  to  $10^{-4}$  hPa ( $z \sim 90$ – $110$  km, not shown).

Since it is unlikely that the resolved eastward GWs in the upper mesosphere and lower thermosphere at middle and high latitudes could have originated in the troposphere, unless their eastward phase speeds are very large ( $>120 \text{ m s}^{-1}$ ) in order to propagate through the polar night jet, we hypothesize that these eastward GWs are secondary GWs that are generated in the stratosphere and lower mesosphere. This notion is further supported by the fact that the momentum flux reversal around 0.003 hPa ( $z \sim 85$  km) in Figure 3e is accompanied by an increase in the potential energy flux and a separate high-altitude energy deposition maximum (Figure 3g). Again, these features are absent in the conventional T32L80 model.

Figure 4 shows latitude-height cross sections of the zonal and temporal means of the potential energy flux density and the energy flux density (see equations (4) and (7)). In the NH (summer), there is some increase of the potential energy flux density with altitude in the region where the westward mean zonal wind increases with altitude. This is because of the increasing difference between the dominating eastward GW phase speeds and the westward mean zonal wind (see the second theorem of Eliassen and Palm mentioned earlier in this section). Otherwise, both flux densities decrease monotonically with altitude as a result of wave dissipation. Both flux densities also decrease with altitude in the SH (winter) above about 60 km. In addition, the potential energy flux density increases with height below the polar night jet maximum; again this is a consequence of second theorem of Eliassen and Palm. However, there is a significant negative (downward) energy flux in the stratosphere around  $60^\circ\text{S}$ , whereas the potential energy flux is upward everywhere. This feature can be

explained as follows. The westward GW drag in the SH in the stratosphere and lower mesosphere is mainly due to orographically generated GWs or nonorographic GWs with slow ground-based phase speeds. Though these waves have a positive (upward) potential energy flux, their total energy flux is zero or only weakly positive. Secondary GWs generated by intermittent orographic GW drag have significant ground-based phase speeds and propagate vertically in both directions with significant energy fluxes. The downward propagating secondary GWs then cause a negative (downward) energy flux in the mean. This interpretation is consistent with the finding of Sato et al. (2012) that even the potential energy flux can temporarily be downward in the austral winter stratosphere. Also note that the energy flux density of parameterized GWs is positive definite; it either is constant or decreases with altitude above the launch level.

The results from our zonal-mean diagnostics are strongly indicative that secondary GWs play a vital role for the general circulation in the SH winter mesopause region. In the next section we analyze the simulated reversal of the GW momentum flux and drag with altitude in more detail.

## 4. Detailed Analysis of Resolved GWs in the SH

### 4.1. Geographical Distribution and Relative Importance of Orographic GWs

In the following we consider the geographical distribution of the simulated GW activity. Figure 5 shows the momentum and energy flux densities at 20 km for the three spectral ranges defined in the previous section. At this altitude, the GW fluxes include orographically generated GWs that are filtered by the tropospheric large-scale winds, as well as GWs that are generated in the upper troposphere by imbalances associated with baroclinic Rossby waves. GW generation by the spatially and temporally variable latent heating (parameterized as large-scale condensational heating and moist convection) is also simulated but is of minor importance at higher latitudes in austral winter. Figure 5 shows that all three spectral ranges contribute to the GW fluxes at 20 km, although medium and large-scale GWs ( $\lambda_h \sim 200\text{--}1,350$  km) provide the largest contributions. There are six major GW hot spots in Figure 5: the subtropical peak of the Andes, the Antarctic Peninsula, the Southern Andes, New Zealand, Tasmania, the Ross Ice Shelf, and the southeastern edge of Africa. The source mechanism for all these hot spots is presumably flow over orography, except for the Ross Ice Shelf where the generation is caused by katabatic winds (Watanabe et al., 2006). The locations of these hot spots compare well with observational results of Hendricks et al. (2014), as well as with modeling results of Sato et al. (2012). We conclude that orographic GWs relevant for the middle atmosphere are reasonably well simulated with the KMCM. However, the orographic GWs will be spectrally biased, especially at lower altitudes, since a T240 resolution misses small-scale orographic GWs with  $\lambda_h < 165$  km (see also the discussion in Alexander & Teitelbaum, 2011).

The relative importance of the orographic GWs for the primary zonal-mean GW drag can be estimated by considering certain longitude sectors where orographic generation is dominant. According to Sato et al. (2012), this includes also some area downstream of the orographic source regions. Accordingly, we average from 90°W to 30°W and from 160°E to 160°W to obtain a rough estimate for orographically generated GW fluxes from the Southern Andes/Antarctic Peninsula region and from the Ross Ice Shelf/New Zealand region, respectively. Figure 6 shows the absolute momentum flux (MF, see equation (6)) and the zonal momentum flux ( $F_{zz}$ , see equation (3)) for the orographic and nonorographic regions at 20 km (dashed black and solid grey curves). These contributions are weighted with the corresponding longitude sectors such that their sum equals the corresponding zonal-mean flux (solid black curves). The zonal-mean MF compares quantitatively well with the model data compiled by Geller et al. (2013, their Figure 2) for July. The MF simulated with the KMCM is about twice as strong as the corresponding result from the KANTO model (see Alexander et al., 2016, their Figure 8d). Though the nonorographic regions dominate MF in both models, the relative importance of the orographic regions is stronger in the KMCM; this may result partly from differences in the horizontal averaging. The two negative maxima of the dashed black curve around 30°S to 50°S and 70°S in Figure 6b correspond to the latitudes of the orographic sources. At these latitudes, orographic GWs clearly dominate the westward momentum flux entering the middle atmosphere. Nonorographic GWs are dominant around 60°S. This latitude corresponds to the maximum of tropospheric baroclinic Rossby wave activity in the southern winter hemisphere (not shown). We conclude that orographic and nonorographic GWs yield approximately equal contributions to the zonal-mean westward GW drag in the austral winter stratosphere and lower mesosphere. However, since orographic GWs show a much higher intermittency than nonorographic GWs (Alexander et al., 2016; Sato et al., 2012), we expect that they are most relevant for the generation of secondary GWs.

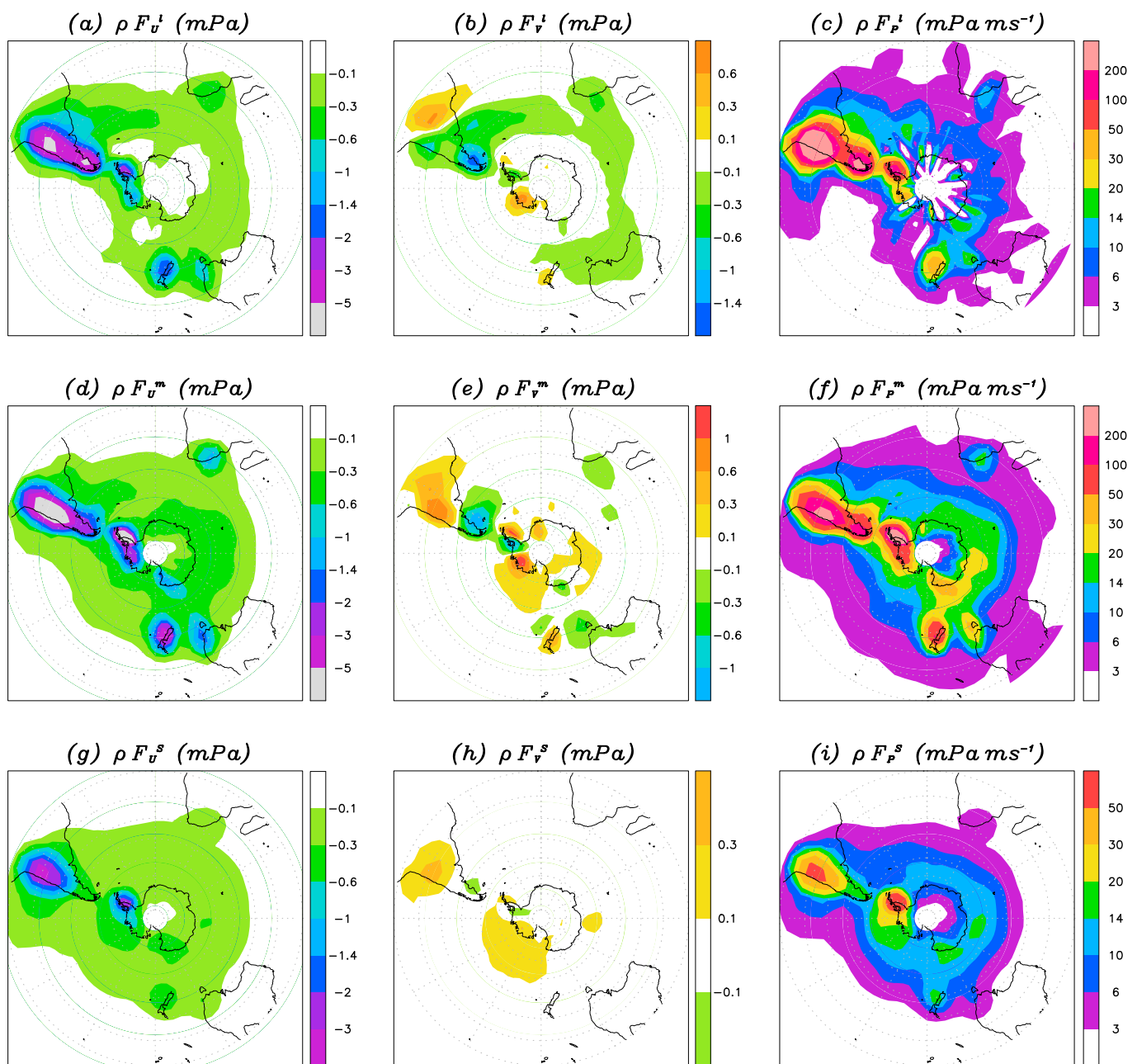


**Figure 5.** Zonal and meridional momentum flux densities (a, d, and g and b, e, and h) and potential energy flux density (c, f, and i) at 20 km. Results are averaged from 21 June to 10 August. Figures 5a–5c, 5d–5f, and 5g–5i show contributions from large-scale, medium-scale, and small-scale GWs, respectively (see equations (1) and (2)).

#### 4.2. Longitude-Height Structure and Intraseasonal Variability

Since the maximum GW drag in the winter middle atmosphere occurs around 60°S, we now consider averages from 50° to 70°S and inspect the longitudinal and vertical structure of the momentum flux and GW drag components (Figures 7a and 7b, see equations (3) and (5)). Figure 7a confirms that the westward GW drag in the SH stratosphere and lower mesosphere during wintertime is concentrated over the Southern Andes and the Antarctic Peninsula. A second maximum of the westward GW drag is centered at ~165°E and is presumably linked to the GW hot spots over New Zealand and the western edge of the Ross Ice Shelf.

Figure 7a indicates a reversal of the momentum flux in the mesosphere that occurs downstream of the westward maxima. This is consistent with the hypothesis that mainly orographically generated GWs with small ground-based phase speeds give rise to the westward drag in the stratosphere and lower mesosphere

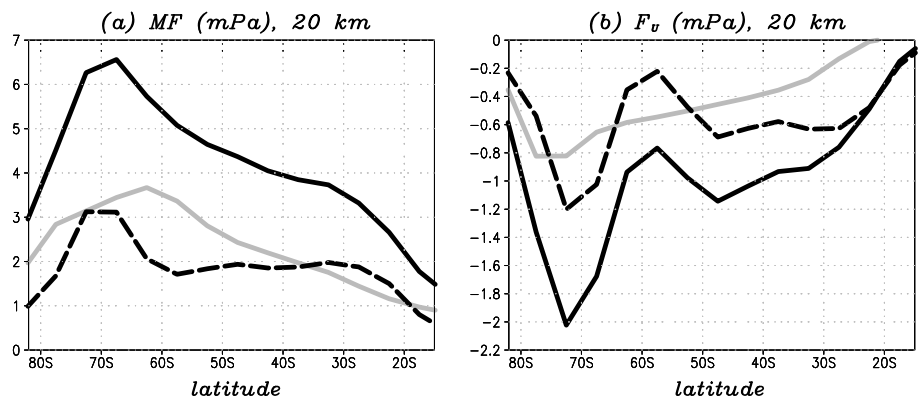


**Figure 6.** Absolute (a) and zonal (b) momentum fluxes in the southern hemisphere at 20 km according to equations (6) and 3, respectively, and averaged temporally from 11 June to 10 August. The dashed black and solid grey curves correspond to the contributions from orographic and nonorographic regions, respectively (see text for definitions). The solid black curves correspond to the zonal-mean fluxes.

and that secondary GWs with significant ground-based phase speeds give rise to the eastward momentum flux and drag in the upper mesosphere. The latter propagate upward and horizontally, mainly to the east and to the west relative to the mean zonal wind in the secondary GW source regions; these source regions are located in regions of maximum westward GW drag. Since the mean zonal wind is eastward and decreases with altitude in the mesosphere up to the region of the aforementioned secondary wind maximum, the relative mean wind is therefore “westward” at higher altitudes in the frame of reference of the wind at the altitude where the secondary GWs are generated. This causes the upward eastward secondary GWs to attain longer vertical wavelengths than the upward westward secondary GWs and therefore allows the eastward GWs to propagate to the higher altitudes before dissipating.

The meridional momentum flux and GW drag (Figure 7b) shows variations with longitude and height that are similar to that of the zonal components, with weak poleward (southward) flux and drag in the stratosphere and lower mesosphere, and a strong equatorward (northward) flux and drag in the upper mesosphere. The northward drag in the upper mesosphere is presumably due, in part, to secondary GWs. It contributes significantly to the zonal-mean meridional momentum budget, that is, it modifies the thermal-wind relation. In the SH, the geostrophic balance for the zonal-mean zonal wind in pressure coordinates is modified by the meridional GW drag according to

$$|f| [u] \approx a^{-1} [\partial_\phi \Phi] - [\text{GWD}_v]. \tag{11}$$

There is low geopotential height in the stratosphere and lower mesosphere over the pole during wintertime. Hence, the first term on the right-hand side of equation (11) is positive, implying an eastward flow. As mentioned earlier, the additional eastward wind maximum in the upper mesosphere is related to the fact that the temperature decreases toward the pole in a region around 0.0001 hPa ( $z \sim 110$  km). In contrast, the result from conventional middle atmosphere climate models is that there is an increase of the temperature toward the pole in this region. A temperature decrease with latitude in the polar mesopause region, however, amplifies the low over the pole and therefore implies enhanced eastward flow. If the second term in equation (11) is negative, as is the case based on Figure 7b, the additional zonal wind maximum is reduced by the meridional GW drag. We have  $|f| [u] \sim 300 \text{ m s}^{-1} \text{ d}$  and  $[\text{GWD}_v] \sim 60 \text{ m s}^{-1} \text{ d}$  in the region of the additional maximum of the zonal wind. Hence, the wind maximum is reduced by about 20% due to the northward meridional GW drag.

Figure 7c shows the temporal evolution of the zonal momentum flux averaged from 80°W to 20°W and from 50°S to 70°S. The longitudinal average captures the major westward maximum in the stratosphere and lower mesosphere, as well as the strong eastward momentum flux farther downstream in the upper mesosphere (see Figure 7a). The time series of daily mean values shows intraseasonal variability with a time scale of about 10 days which is typical for baroclinic Rossby waves. This is consistent with the assumption that the primary GWs in this region are mainly generated by large-scale flow over steep orography. An event of maximum westward momentum flux in the stratosphere (and strong reversal higher up in the mesosphere) occurs

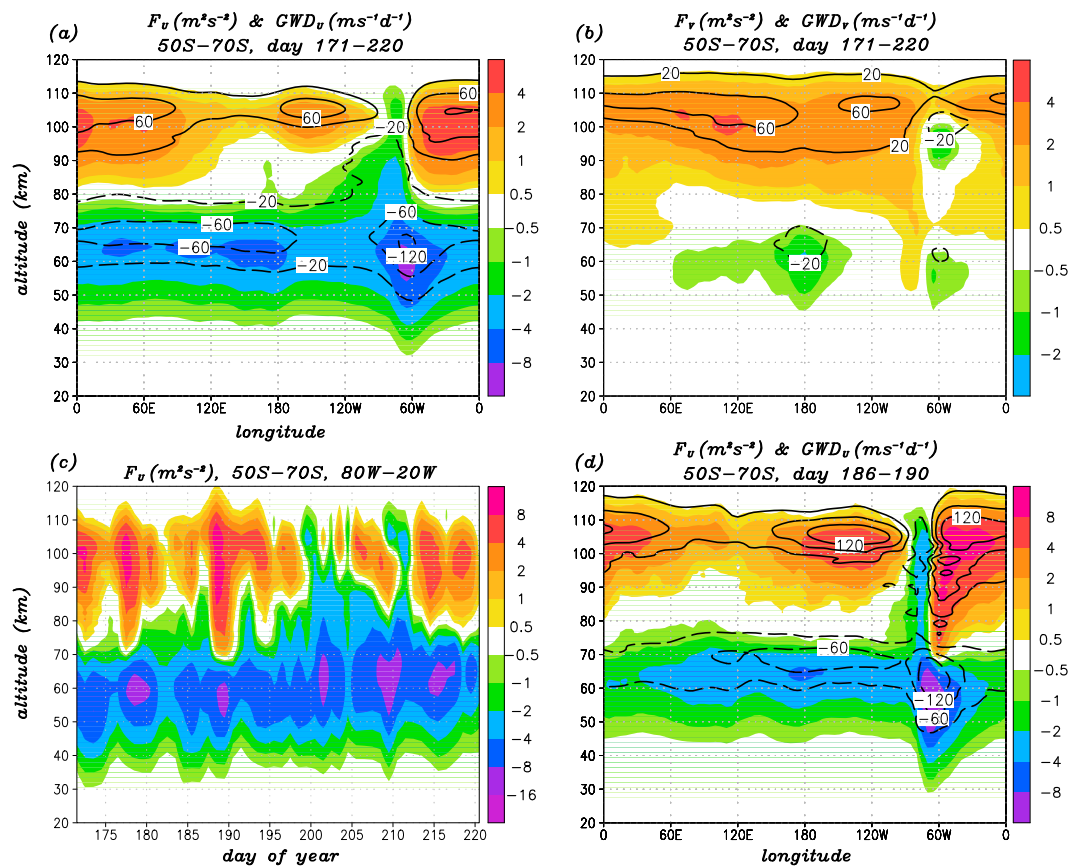


**Figure 7.** (a) Gravity wave (GW) zonal momentum flux ( $F_u$ , colors) and drag ( $GWD_u$ , contours), averaged from 50°S to 70°S and from 21 June to 10 August. (b) Same as (a) but for the meridional momentum flux and drag. (c) Temporally resolved (1 day consecutive averages) of  $F_u$  averaged from 50°S to 70°S and from 80°W to 20°W. (d) Same as (a) but for the temporal average from 6 to 10 July. The vertical coordinate is geometric height above sea level. See equations (3) and (5) for definitions.

from about 6–10 July (days 186–190). Comparing Figure 7d to Figure 7a confirms that the 6–10 July temporal average yields basically the same longitudinal distribution of the zonal GW flux as the average over the whole 50 day time period. Although the GW effects over the Southern Andes, the Antarctic Peninsula, and the region north of the Ross Ice Shelf are somewhat stronger for the 6–10 July event than for the full 50 day average, we assume that the 6–10 July event is typical for the simulated GW dynamics in the southern winter middle atmosphere. In the next subsection we analyze this event in more detail.

### 4.3. Geographical and Short-Term Variability of the Local GW Drag Components

Figure 8 shows the geographical distribution of the vertically averaged zonal and meridional GW drag components using equation (5). Here we average over the 5 day time interval from 6 (0 UT) to 10 (24 UT) July, and we vertically average from 40 to 70 km (Figures 8a and 8b) and from 70 to 110 km (Figures 8c and 8d) using density weighted averages. Since the zonal-mean GW drag is comparatively weak in the subtropics of the middle atmosphere (see Figure 3e), we show the regions poleward of 35°S only. There are three regions of strong westward zonal body force in Figure 8a: (1) the Southern Andes (around 50°S, 70°W), (2) the Antarctic Peninsula (around 70°S, 50°W), and (3) the region west of the Ross Ice Shelf (around 75°S, 165°E). Figure 8b shows that the same regions are also characterized by local maxima of the meridional GW drag. The meridional GW drag is southward in region (1) and northward in regions (2) and (3). Though the primary GWs propagate mainly westward relative to the mean flow, as is expected, they also have meridional components that partly average out in the zonal mean.

Comparing Figures 8a and 8c demonstrates again that the change in the direction of zonal GW drag at mesopause altitudes occurs downstream of the westward drag maxima in the  $z = 40\text{--}70$  km region. Furthermore, there is some westward drag in the mesopause region over the Southern Andes and the Antarctic

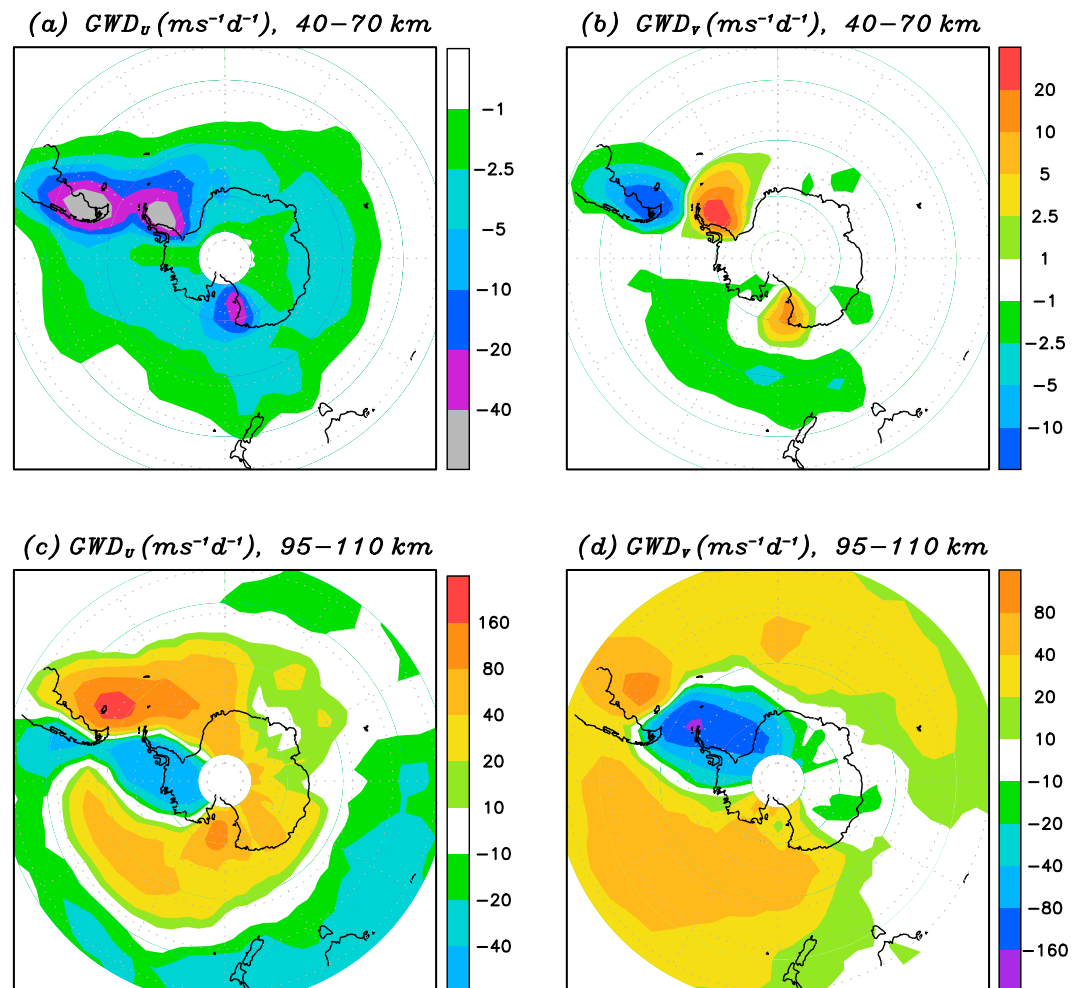


**Figure 8.** Geographical distribution of the zonal and meridional gravity wave drag components using equation (5). The zonal and meridional gravity wave drag components are averaged temporally from 6 to 10 July and are averaged from  $z = 40\text{--}70$  km (a and b) and from  $z = 95\text{--}110$  km (c and d) using density-weighted vertical averaging.

Peninsula that extends upstream relative to these hot spots. The meridional GW drag also changes sign from the 40–70 km region to the mesopause region over the Southern Andes and over the Antarctica Peninsula (Figures 8b and 8d). The structure and strength of the meridional GW drag in the mesopause region (Figure 8d) indicates that the secondary GWs propagating away from the Southern Andes and the Antarctic Peninsula in zonal direction have significant poleward components to the south and equatorward components to the north. Assuming an idealized mean flow, Vadas et al. (2003, their Figures 9 and 10) found that the secondary GWs from a body force have cone-like distributions of propagation directions which are centered both parallel and antiparallel to the body force direction created by the primary GWs. Such a behavior is fully reflected by the situation illustrated in Figure 8 above the Southern Andes and the Antarctic Peninsula.

In the mesopause region over the Ross Ice Shelf, however, the simulated GWs account only for an eastward drag along with some weak equatorward component. A closer inspection of the model data showed westward mean flow around 70 km in region (3) such that westward GWs generated at lower altitudes cannot reach the mesopause region.

The hypothesis of secondary GWs in the mesopause region can be further tested by considering the temporal correlation between the drag maxima in the stratopause and mesopause regions. More specifically, we shall consider the short-term temporal evolution of the GW drag. In addition, we take into account the horizontal propagation that would accompany the vertical propagation according to Figure 8. Figures 9g–9i shows time series from 6 July at 1:30 UT to 10 July at 22:30 UT of the zonal GW drag from the upper stratosphere to the midmesosphere for the three regions of interest. From left to right, we average horizontally over 45°S–55°S

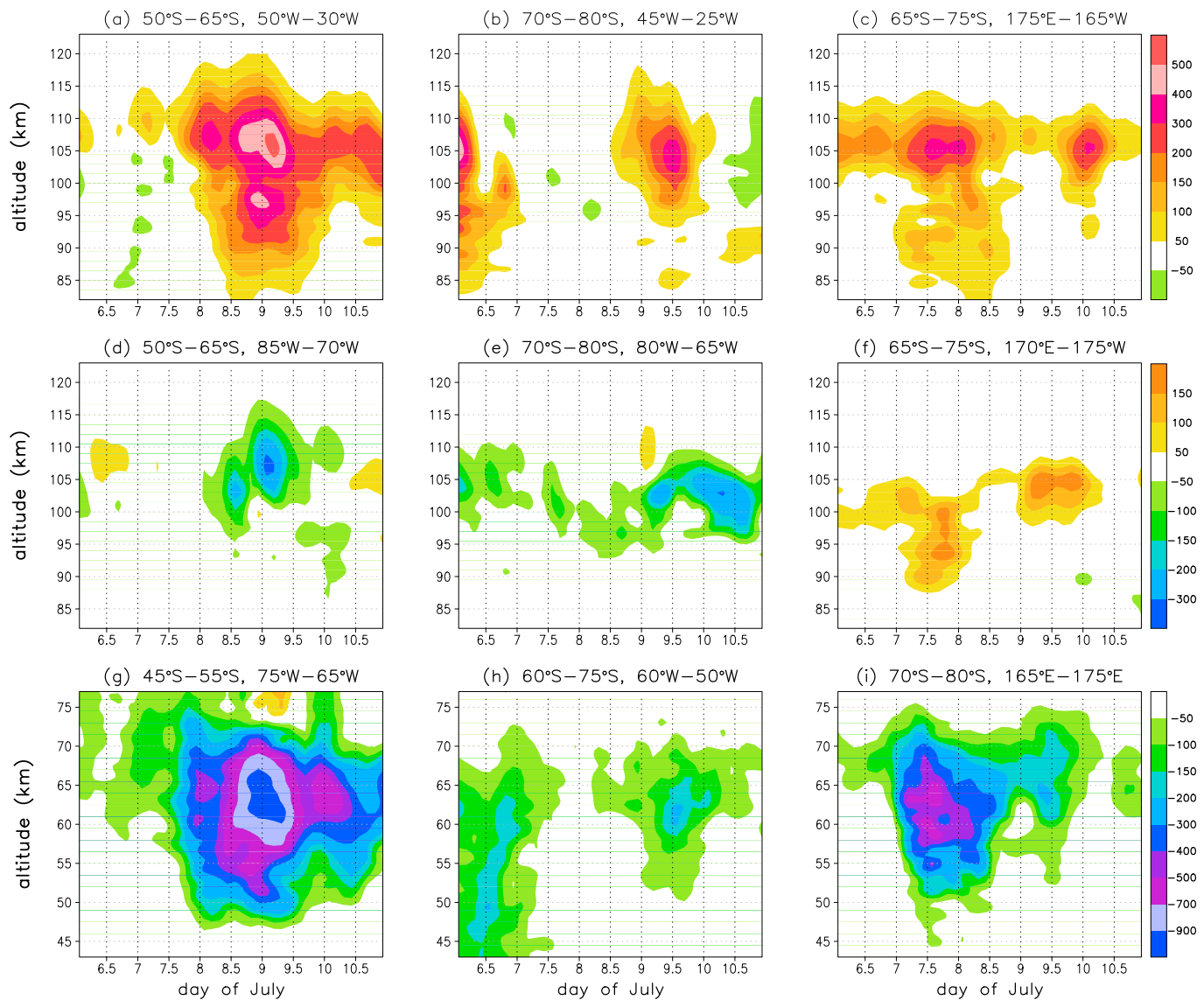


**Figure 9.** Time series of the zonal GW drag per unit mass ( $GWD_u$ , see equation (5), the unit is  $m s^{-1} d^{-1}$ ) in the stratopause region (g–i) and in the mesopause region (d–f and a–c) from 6 (1:30 UT) to 10 (22:30 UT) July. The time series is based on consecutive 3 h averages. The drag is furthermore averaged over certain horizontal domains (see the panel titles). The vertical coordinate is geometric height above sea level.

and  $75^{\circ}W-65^{\circ}W$  for the Southern Andes (region (1)),  $60^{\circ}S-75^{\circ}S$  and  $60^{\circ}W-50^{\circ}W$  for the Antarctic Peninsula (region (2)), and  $70^{\circ}S-80^{\circ}S$  and  $165^{\circ}E-175^{\circ}E$  for the western edge of the Ross Ice Shelf (region (3)). Distinct maxima of westward GW drag are evident around 9 July in region (1), around 9.5 July in region (2), and around 7.5 July and 9.5 July in region (3). We now ask whether these westward drag maxima coincide roughly with eastward or westward GW drag maxima in the mesopause region (taking into account the horizontal displacement consistent with the horizontal direction of propagation according to Figure 8).

Figures 9a–9c show the GW drag in the mesopause region downstream of the regions shown in Figures 9g–9i. We average over  $50^{\circ}S-65^{\circ}S$  and  $50^{\circ}W-30^{\circ}W$  for region (1),  $70^{\circ}S-80^{\circ}S$  and  $45^{\circ}W-25^{\circ}W$  for region (2), and  $65^{\circ}S-75^{\circ}S$  and  $175^{\circ}E-165^{\circ}W$  for region (3). The eastward GW drag maxima in the mesopause region occurs approximately at the same time as the westward maxima near the stratopause. For the event on 9.5 July in region (3) we can infer a temporal delay of several hours (compare Figure 9c to Figure 9i).

Figures 9d and 9e also show the GW drag in the mesopause region, but somewhat upstream of the primary GWs regions. We average over  $50^{\circ}S-65^{\circ}S$  and  $85^{\circ}W-70^{\circ}W$  for region (1) and  $70^{\circ}S-80^{\circ}S$  and  $80^{\circ}W-65^{\circ}W$  for region (2). Since the westward secondary GWs have smaller intrinsic frequencies, the propagation time

from the stratopause to the mesopause region is longer than for the eastward secondary waves. This reasoning is confirmed by comparing the timing of the westward GW drag maxima in Figures 9d and 9e to those in Figures 9g and 9h. For example, the main event on 9.0 July in Figure 9g is followed by a westward drag maximum in Figure 9d that occurs a few hours later. In region (2), the delay between the primary event on 9.5 July and the secondary maximum in the mesopause region is almost 1 day. Also note that the westward GW drag maxima in the mesopause region are much weaker than the corresponding eastward maxima.

Figure 9f refers to region (3) in the upper mesosphere. Here we chose a horizontal displacement about half of that used in Figure 9c. Comparing with Figure 9c, the eastward drag maxima corresponding to the primary events on 7.5 and 9.5 July occur earlier and at a lower altitude. This is consistent with the assumption of GW packets propagating away from the source region. Due to continuous dissipation of GW energy along the path of the wave packet, the wave drag is expected to occur later and at a higher altitude when probing a vertical column farther away from the source region.

Summarizing, the features deduced from Figures 8 and 9 agree well with the hypothesis that the net zonal-mean eastward GW drag in the mesopause region discussed in section 3 is due to secondary GWs that are generated in the stratosphere and lower mesosphere according to the mechanism proposed in Vadas et al. (2003). The secondary GWs are expected to have zonal phase speeds of tens  $\text{m s}^{-1}$  relative to the mean wind at the source level. Since the mean zonal wind decreases with altitude in the mesosphere (up to the regime of the additional wind maximum), the westward secondary GWs have shorter vertical wavelengths and smaller vertical group velocities than the eastward secondary GWs. As a result, the westward secondary GWs are more susceptible to dissipation in the mid mesosphere than the eastward secondary GWs. The westward secondary GWs also exert a weaker drag around the mesopause which occurs later in time as compared to the drag exerted earlier by the eastward secondary GWs.

#### 4.4. GW Phases and Interaction With Tides

Figure 10 shows subsequent horizontal cross sections of the vertical wind at 10 hPa ( $z \sim 30$  km) around 9 July over the Southern Andes. A quasi-stationary GW packet with high amplitudes is evident. Farther downstream, this GW packet shows propagation away from the orographic source region. Such a feature is also known from satellite observations and other high-resolution models (e.g., Alexander & Teitelbaum, 2011; Sato et al., 2012). The fact that the GW phases in the stratosphere are quasi-stationary confirms that these GWs are indeed orographically generated. The simulated scales in the stratosphere are only somewhat larger than in regional models that are run at much higher resolution than the KMCM (see Alexander & Teitelbaum, 2011, their Figures 4 and 5). Downstream of the Southern Andes, Figure 10 indicates the development of smaller structures with phases that are inclined at an angle with respect to the phases of the primary orographic GWs. Such structures are a well-known result of GW instability (e.g., Fritts & Alexander, 2003). In the real atmosphere this leads to even finer structures and to turbulence. The initial part of this energy cascade is resolved by the present model, while the major part of the energy cascade is represented by the turbulent diffusion scheme.

Figure 11 shows subsequent horizontal cross sections of the vertical wind around 9 July at 0.01 hPa ( $z \sim 80$  km). A clear picture of the main propagation directions of the GWs cannot be deduced from these plots; overall, the GW phases look more complicated and less structured than in Figure 10. This is because the mean wind (indicated by black arrows) is quite variable. This variability is caused by eastward planetary waves and, particularly, by westward propagating thermal tides. It induces variations of the ground-based phase speeds of the GWs according to the ray trace equations.

The most striking difference between Figures 11 and 10 is that the GW phases in the mesosphere are no longer indicative of orographic GWs. This is further illustrated in Figure 12 by showing longitude-time cross sections of the GW-related zonal wind perturbations at 10 hPa ( $z \sim 30$  km) and  $52^\circ\text{S}$ , and at 0.01 hPa ( $z \sim 80$  km) and  $60^\circ\text{S}$ . Stationary (orographic) GWs are evident in Figure 12a with zonal wavelengths of  $\lambda_h \sim 400$  km. The eastward and westward propagating waves at 0.01 hPa (Figure 12b) have dominant zonal wavelengths that are more than twice as long as in Figure 12a, as can be seen via the black lines. While the ground-based periods of the westward secondary GWs are quite long (about 10 h), the dominant period of the eastward waves is about 4–5 h. Together with a wavelength of about 1,200 km, we obtain a zonal phase speed of about  $70 \text{ m s}^{-1}$ . Such GWs cannot be of tropospheric origin since they would not have survived the dynamic instability (or critical levels) when propagating through the polar night jet, which on average has zonal wind speeds of more than  $140 \text{ m s}^{-1}$  east of the Southern Andes at  $\sim 50$  km (not shown). Instead, these GWs must have been generated above the polar night jet maximum where the mean wind is smaller than the ground-based phase

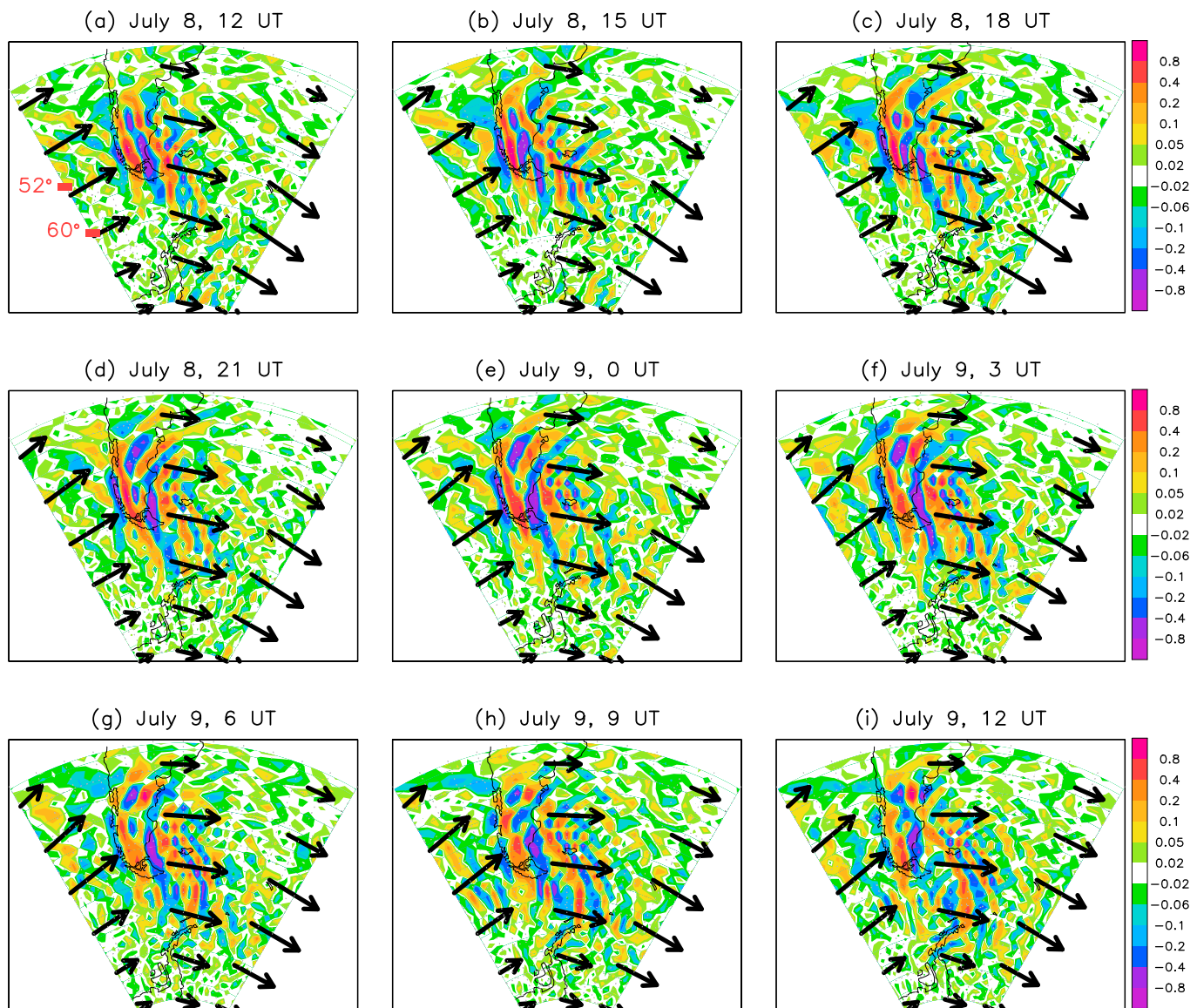


**Figure 10.** Consecutive snapshots of the GW-related vertical wind perturbation (computed according to  $w' = -(g\bar{\rho})^{-1}\omega'$ ) at 10 hPa (~30 km) above the Southern Andes around 9 July (color shading, the unit is  $\text{m s}^{-1}$ ). The horizontal mean flow is indicated by arrows and has a maximum value of  $95 \text{ m s}^{-1}$ . The latitudes  $52^\circ\text{S}$  and  $60^\circ\text{S}$  are marked in red in (a).

speed. This is the case above about 0.1 hPa (~60 km) in the region of the Southern Andes. Furthermore, the fact that the GWs in the upper mesosphere have larger horizontal wavelengths than the primary orographic GWs is consistent with the concept of secondary GW generation as proposed by Vadas et al. (2003).

Radar observations and model simulations show that the semidiurnal tidal wind variations in the MLT give rise to significant modulation of GW amplitudes and GW-mean flow interaction (Becker, 2012, 2017; Beldon & Mitchell, 2010; Kinoshita et al., 2015). This mechanism applies also to the simulated secondary GWs in the austral winter polar mesopause region. Figure 13 demonstrates that the eastward GWs that propagate into the mesopause region downstream of the Southern Andes are absorbed due to dynamical instability and critical levels imposed by the large-scale zonal wind and that this wind shows considerable variability associated with the semidiurnal tide. According to the usual dynamic instability criterion for GWs, we observe strong eastward GW drag during the development of the eastward phase of the zonal wind tide. Before the time of the maximum eastward GW drag (i.e., from 6 to 8 July), the large-scale zonal wind also shows westward winds during the tidal minima. When these minima develop, westward propagating GWs are damped

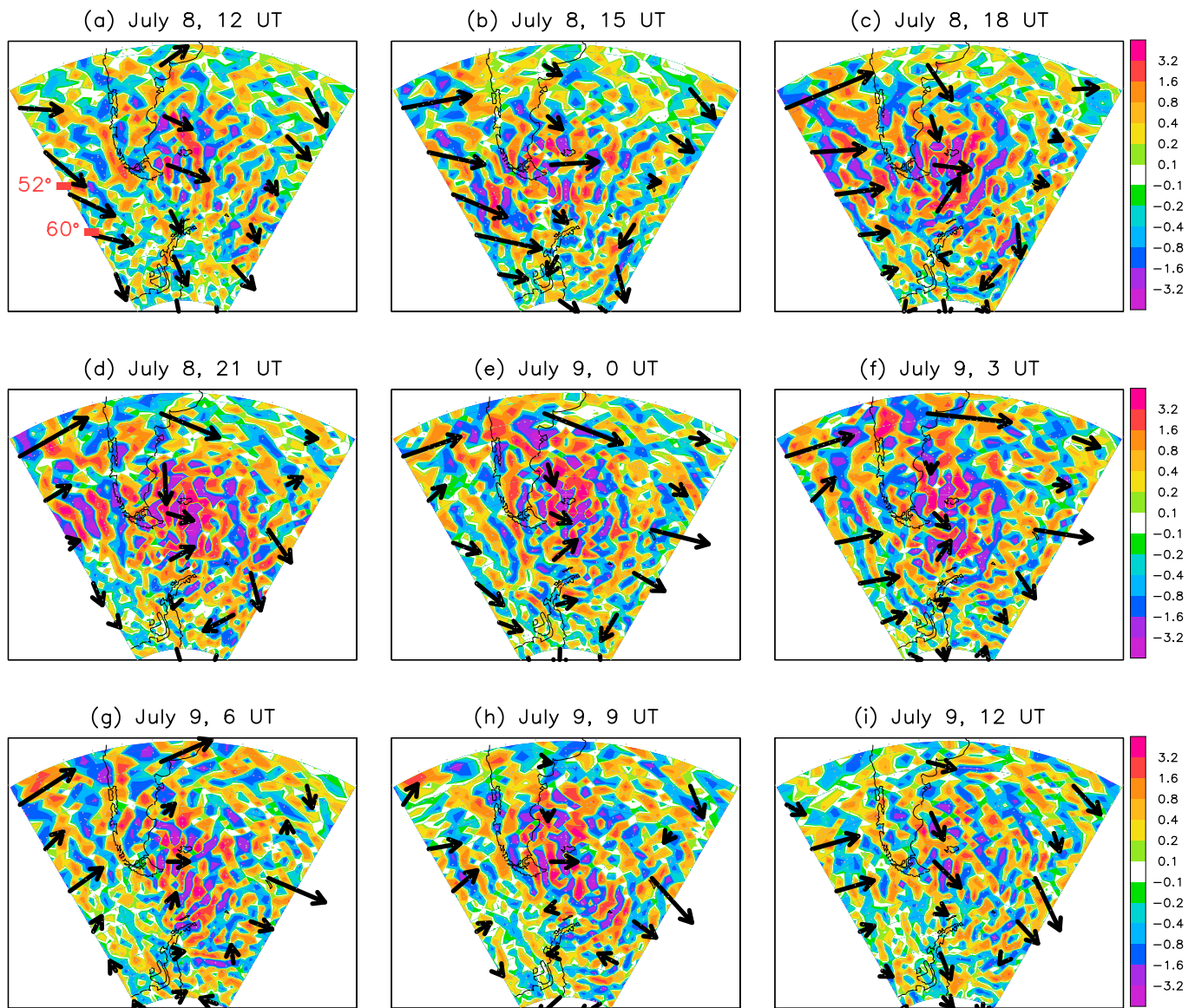


**Figure 11.** Same as Figure 10 but for 0.01 hPa ( $z \sim 80$  km). The horizontal mean flow has a maximum value of  $140 \text{ m s}^{-1}$ . Note the different color bar compared to Figure 10.

and give rise to a westward GW drag. Figure 13 also illustrates that the strong eastward drag around 9 July induces a significant temporary acceleration of the large-scale mean zonal wind.

In the lower thermosphere we observe eastward drag during the westward phase of the tide. This is an artifact of the sponge layer; that is, all GWs are strongly damped by horizontal diffusion around  $3 \times 10^{-5}$  hPa ( $z \sim 130$  km). In the real atmosphere, the eastward GWs would propagate to somewhat higher altitudes until being absorbed by the eastward phase of the zonal wind tide. Hence, we expect that the additional maximum of the zonal-mean zonal wind as simulated using the present model version will extend to somewhat higher altitudes if the model top and the sponge layer are raised.

**4.5. Observational Evidence**

As mentioned in section 1, the persistently strong amplitudes in the temperature variations as observed by Chen et al. (2016) over McMurdo (Antarctica) during the wintertime, and their correspondingly different vertical scales as compared to the stratospheric observations of Zhao et al. (2017) at the same site, cannot be explained using conventional GCMs with parameterized GWs. Additionally, Zhao et al. (2017) infer horizontal wavelengths of  $\lambda_h \sim 350\text{--}500$  km in the stratosphere, while Chen and Chu (2017) and Chen et al. (2013)

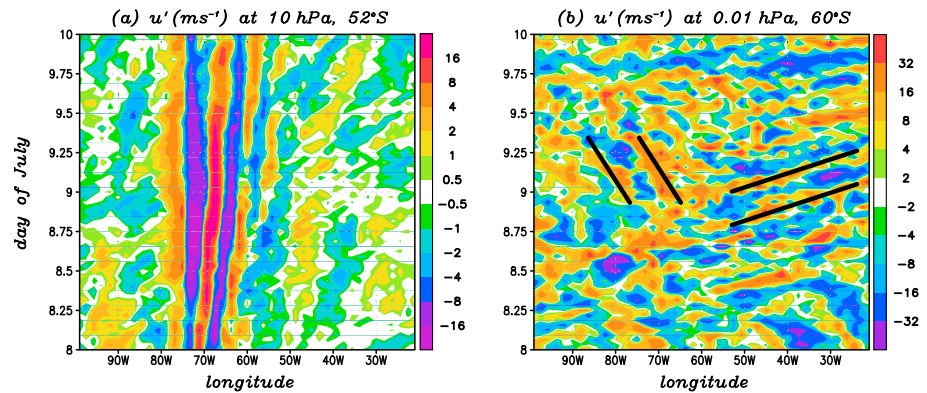


**Figure 12.** Longitude-time cross sections of the GW-related zonal wind perturbation ( $u'$ ) in the stratosphere at 10 hPa ( $z \sim 30$  km) at  $52^\circ\text{S}$  (a) and in the mesosphere at 0.01 hPa ( $z \sim 80$  km) at  $60^\circ\text{S}$  (b). Eastward and westward GW phases are indicated by black lines in (b). Note the different color scales in the two panels.

infer horizontal wavelengths of  $\lambda_h \sim 800\text{--}3,000$  km in the upper mesosphere. Such different horizontal wavelengths separated by only  $\Delta z \sim 30\text{--}50$  km in altitude implies that the GWs observed at  $z \sim 30\text{--}50$  km are not the same GWs as those observed at  $z \sim 80\text{--}100$  km. Figure 14 compares the observed GW-related relative temperature variations during late June over McMurdo from Chen et al. (2016, their Figure 2) to corresponding results from our KMCM simulation. The amplitudes (up to  $\sim 16\%$  in the MLT) and periods of the simulated temperature variations (Figure 14b) compare well with the lidar data (Figure 14a). Moreover, the characteristic change from short vertical wavelengths in the stratosphere to long vertical wavelengths in the upper mesosphere as seen in the observational data agrees well with the model. In this context we note that Vadas et al. (2003) predict that secondary GWs generated by the intermittent body forces of primary GWs have longer horizontal and longer vertical wavelengths than those of the primary waves. This is consistent with both the observations and the model results. On the other hand, the GW-induced temperature variation deduced from the nonorographic GW scheme in the conventional model setup amounts only to 3% around the polar winter mesopause, and this result is at least partly an artifact because of nearly horizontally uniform launch level parameters in the troposphere.

As mentioned in section 1, the recent analysis by de Wit et al. (2017) of meteor radar measurements east of the Southern Andes revealed persistent eastward GW momentum flux during wintertime in the mesopause

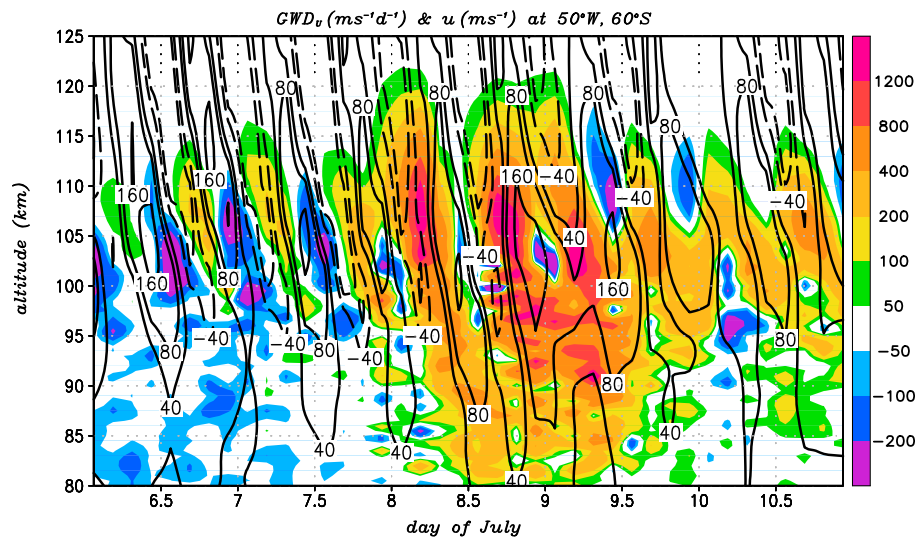


**Figure 13.** Height-time cross section of the zonal GW drag (colors) and the mean zonal wind (black contours) southeast of the Southern Andes. The time interval extends from 6 (1:30 UT) 10 (22:30 UT) July. The vertical coordinate is height above sea level.

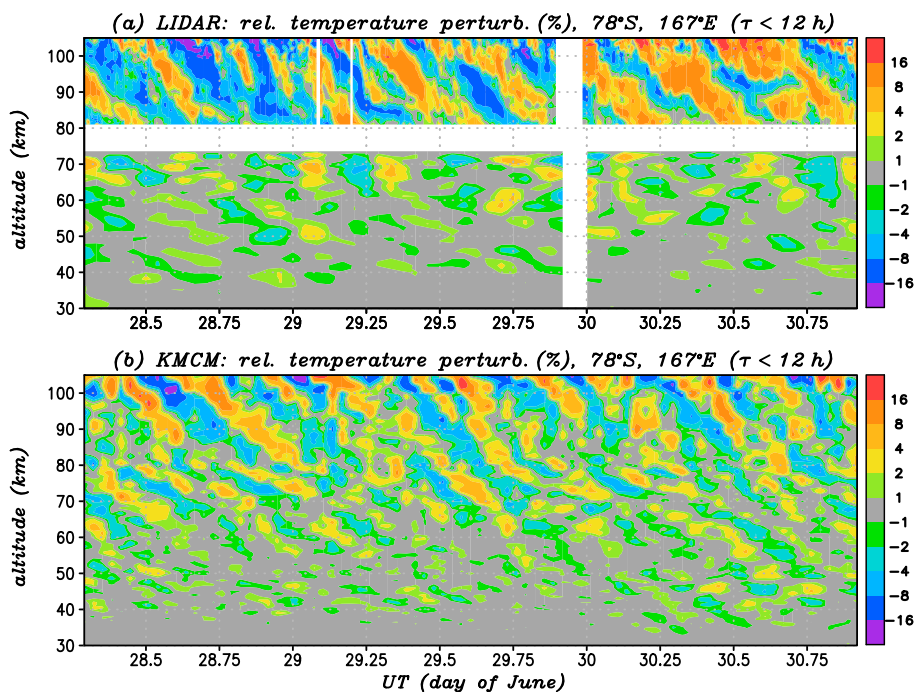


**Figure 14.** GW-related relative temperature perturbations at the site of McMurdo (Antarctica) during late June. The perturbations are calculated as  $(T - \bar{T})/\bar{T}$  where  $\bar{T}$  includes only periods of 12 h or longer. (a) From ground-based lidar measurements as published in Chen et al. (2016, their Figure 2). These data were kindly provided by X. Chu. (b) From the Kühlungsborn mechanistic general circulation model (KCGCM) simulation. LIDAR = Light Detection and Ranging.

region. This finding is consistent with our model result of the regional distribution of the zonal GW drag (see Figure 8c). Additionally, consistent with our model study, the authors interpreted their result as due to secondary GW generation in the stratopause region that resulted from the strong and intermittent GW breaking over the Southern Andes hot spot.

Further observational support is available from radar wind measurements in the NH. On average, the polar night jet is much weaker in the NH than in the SH. A strong polar night jet, however, creates the conditions for

primary westward GWs to gain high amplitudes when they break in the upper stratosphere and lower mesosphere, thus exciting secondary GWs which can then dissipate at higher altitudes. Figure 15 shows winds from Modern-Era Retrospective analysis for Research and Applications (MERRA) (Rienecker et al., 2011) at 68°N. The mean winds from 2004 to 2016 peak at  $z \sim 40\text{--}50$  km and are eastward with an amplitude of  $\sim 30$  m s<sup>-1</sup>. However, the 2015–2016 winter season was characterized by a very strong polar vortex, especially from 15 to 22 January. During this period, the eastward winds had peak values of  $\sim 110$  m s<sup>-1</sup>. Following our model results we expect a strong additional wind maximum near the mesopause during this period. Importantly, the radar observations included in Figure 15 are consistent with this picture. The Andenes meteor radar is located in northern Norway and measures the horizontal winds in the mesopause region (Stober et al., 2012). From Figure 15, the average wind at  $z \sim 90\text{--}100$  km was  $\sim +10$  m s<sup>-1</sup> during 2004–2016. However, from 15 to 22 January in 2016, a pronounced additional eastward wind maximum of  $\sim 30\text{--}40$  m s<sup>-1</sup> is seen at  $z \sim 95$  km. The altitude and magnitude of this eastward wind maximum is similar to that from our model results for the SH. Though the winds at a single station do not represent the zonal-mean picture, we nevertheless speculate that stationary planetary waves do not significantly contaminate the result.

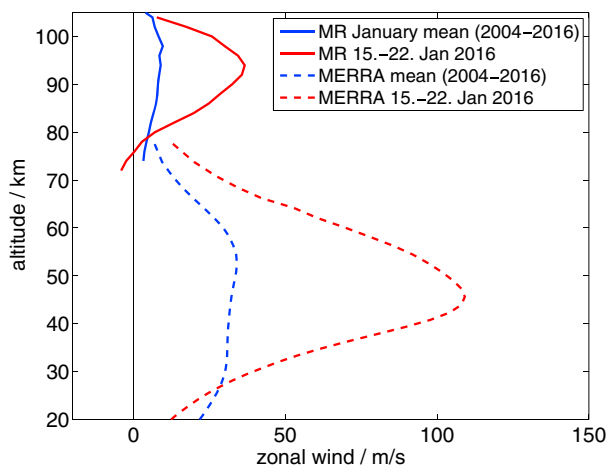


**Figure 15.** Mean zonal wind profiles above Andenes (69°N, 17°E) during January. The blue curves are the mean values for 2004–2016. The red curves correspond to the period 15–22 January in 2016. Results from the Andenes meteor radar (MR) are plotted from 75 to 105 km by solid lines, while MERRA data are plotted from 20 to 80 km by dashed lines.

## 5. Summary and Conclusions

In this paper, we utilized a new T240L190 spectral GCM with an advanced macroturbulent diffusion scheme to simulate semirealistic mean flow effects of resolved GWs having  $\lambda_H > 165$  km. This model combines the facilities of previous versions of the KMCM (e.g., Becker, 2009, 2017; Becker & Brune, 2014; Becker et al., 2015; Brune & Becker, 2013). In particular, the new model version resolves intermittent GW packets to a significant degree. For winter conditions in the SH we find that the regional GW drag, even when averaged over several hours and over horizontal domains of a few thousand kilometers, can be 1 order of magnitude larger than in the zonal mean (compare Figures 9 and 3). Using more localized averages, the local body forces turn out to be several orders of magnitude stronger (not shown). According to previous theoretical studies (e.g., Vadas et al., 2003), an intermittent body force generates upward and downward propagating secondary GWs. This process is likely resolved in this model. The results from this model study give rise to a modified view of the general circulation in the austral winter MLT where secondary GWs generated in the stratosphere and lower mesosphere may play a vital role in the upper mesosphere and lower thermosphere.

The picture emanating for the austral winter hemisphere can be summarized as follows: The westward GW drag in the stratosphere and lower mesosphere is largely due to orographic GWs with the main sources being due to flow over the Southern Andes, the Antarctic Peninsula, and New Zealand, as well as winds sloping down onto the Ross Ice Shelf (Figures 5 and 8). The intermittency of the primary orographic GW drag generates secondary GWs with predominantly eastward and westward phase speeds relative to the mean flow in the region where the secondary GWs are generated. Since the mean eastward flow decreases with altitude in the mesosphere, the westward secondary GWs are susceptible to dissipation in the lower and middle mesosphere. The eastward secondary GWs, however, propagate to the mesopause region where they break and deposit their momentum in the eastward phases of the zonal wind tide. This gives rise to a significant eastward GW drag around  $\sim 90$ – $110$  km and  $60^\circ$ S. The drag reverses the residual vertical wind farther poleward, inducing a temperature decrease toward the pole and an additional eastward maximum of the mean zonal wind around  $\sim 100$  km. This feature is not simulated in climate models with GW parameterizations. Such models often instead show a reversal to westward flow at high latitudes in the winter mesosphere at  $\sim 70$ – $80$  km, a feature that is not consistent with available observational data (e.g., Smith, 2012, Figure 2).

The modified view of the general circulation in the mesopause region that results from a GW-resolving model also encompasses the origin of the cold temperatures of the winter polar mesopause. In the present model, these cold temperatures are partly due to the upwelling induced by the eastward GW drag of the secondary GWs. In a conventional model, on the other hand, the cold temperatures are partly determined by the downward heat flux that results when applying the turbulent vertical diffusion coefficient from the nonorographic GW scheme to the resolved flow. The cooling effect due to GW-induced downward heat flux turns out to be much weaker in the present GW-resolving model than in the conventional model setup.

Our analysis of the model data consistently demonstrates that secondary waves are generated in the austral winter stratosphere and lower mesosphere. For example, the potential plus kinetic vertical energy flux density due to the resolved mesoscales turns out to be negative in the stratosphere around  $60^\circ$ S. This can be explained by noting that the energy flux of orographic GWs is close to zero, whereas the secondary GWs have significant ground-based phase speeds and, hence, negative total energy flux below their source region. Considering a particular event of maximum westward (orographic) GW drag around the stratopause over the Southern Andes, we found that eastward and westward secondary GW drag maxima occur in the mesopause region shortly thereafter. These maxima are zonally displaced in the direction of the horizontal propagation of the secondary GWs. Furthermore, the secondary westward drag is weaker and occurs with a greater temporal delay than the eastward drag. This finding is consistent with the fact that for a typical wintertime mesospheric zonal wind profile, the eastward secondary GWs assume greater vertical group velocities and longer vertical wavelengths than the westward secondary GWs.

Nonorographic GWs are not only generated as secondary GWs in the winter middle atmosphere over the orographic GW hot spots, but everywhere at middle latitudes in the troposphere due to the breakdown of baroclinic Rossby waves (Hendricks et al., 2014; O'Sullivan & Dunkerton, 1995). While eastward nonorographic GWs generated in the troposphere cannot propagate through the strong polar night jet, westward nonorographic waves are allowed to propagate to the mesopause region as long as their amplitudes are small enough to avoid dynamic instability at lower altitudes. Our main conclusion about the origin of the eastward GWs is, however, not affected by the possibility that the westward GWs in the mesopause region might be partly of

tropospheric origin. It is also possible that eastward traveling planetary waves in the polar winter mesosphere are a source of inertia GW generation. On the other hand, it is reasonable to assume that the intermittent body forces from primary orographic GWs give rise to the strongest imbalances of the large-scale flow and hence provide the main source for the generation of inertia GWs in the winter middle atmosphere. In addition, the body forces from the dissipation of primary nonorographic GWs likely contribute to the generation of secondary GWs.

Although we did not identify precisely the mechanism of secondary wave generation here, our analysis strongly suggests that the mechanism for emission from imbalance as described in Vadas et al. (2003) applies. This theory solves the time-dependent Eulerian fluid dynamical equations on the  $f$  plane. The equations are linearized about a constant background flow and the momentum equation contains a horizontal body force with finite spatial and temporal extents. In contrast to the more phenomenological theories for GW generation from jets and fronts (see review of Plougonven & Zhang, 2014), the theory of Vadas et al. (2003) yields explicit solutions for the generated GWs and the changes of the large-scale flow induced by the body force. The latter consist of counterrotating horizontal vortices that correspond to the mean flow acceleration by the body force and return flows antiparallel to it. GWs develop in both the exit and the entrance region of the jet stream induced by the body force, and they propagate away from the body force, generating ring-like horizontal structures and fishbone-like structures in time-height cross sections (not shown). It remains to be investigated whether similar theoretical approaches can be used to describe idealized cases of emission from imbalance in the upper troposphere.

We showed that the simulated GW-related temperature variations in the polar mesopause region are quantitatively comparable to lidar observations of Chen et al. (2016) (Figure 14). In particular, the high temperature perturbation amplitudes in the mesopause region as found in our model or in the observations of Chen et al. (2016) cannot be deduced from a GW parameterization model. We also noted that radar wind measurements at high latitudes in the NH during January 2016 showed a pronounced additional wind maximum in the mesopause region during a period of a very strong polar night jet farther below, a situation that is comparable to the usual state in austral winter. Moreover, de Wit et al. (2017) found eastward GW momentum flux around the winter mesopause in meteor radar measurements east of the Southern Andes. Finally, other existing GW-resolving GCMs (Liu et al., 2014; Watanabe & Miyahara, 2009) also show an additional zonal wind maximum in the austral winter polar mesopause region. Hence, the results we show in this paper are consistent with all of these observations and former modeling results.

In conclusion, the most important implication from this study is that the generation and breakdown of secondary GWs in the austral winter middle atmosphere contributes significantly to the general circulation in the MLT region. In follow-up studies we will analyze the intermittency of the primary orographic GWs and the generation mechanism for the secondary GWs in more detail.

#### Acknowledgments

We are grateful to Xinzhao Chu for valuable discussion and providing the lidar data used in Figure 14. We also acknowledge valuable comments by Xian Lu, two anonymous reviewers, and the Editor William Randel. Gunter Stober and Vivien Matthias provided Figure 15 to us. MERRA source data files were acquired from the Goddard Earth Science Data Information Services Center (GES DISC). Model simulations were performed by the authors. Model documentations can be found in section 2 and in the papers that we have cited. The model and lidar data shown in this paper are available via IAP's ftp server at <ftp://ftp.iap-kborn.de/data-in-publications/BeckerJGR2018>. E. B. was supported by the Collaborative Research Centre TRR 181 (subproject T1) funded by the German Research Foundation. S. L. V. was supported by NSF grants PLR-1246405 and AGS-1552315.

#### References

- Alexander, M. J., & Teitelbaum, H. (2011). Three-dimensional properties of Andes mountain waves observed by satellite: A case study. *Journal of Geophysical Research*, *116*, D23110. <https://doi.org/10.1029/2011JD016151>
- Alexander, M. J., Geller, M., McLandress, C., Polavarapu, S., Preusse, P., Sassi, F., et al. (2010). Recent developments in gravity-wave effects in climate models and the global distribution of gravity-wave momentum flux from observations and models. *Quarterly Journal of the Royal Meteorological Society*, *136*, 1103–1124.
- Alexander, S. P., Sato, K., Watanabe, S., Kawatani, Y., & Murphy, D. J. (2016). Southern hemisphere extratropical gravity wave sources and intermittency revealed by a middle-atmosphere general circulation model. *Journal of the Atmospheric Sciences*, *73*, 1335–1349. <https://doi.org/10.1175/JAS-D-15-0149.1>
- Azeem, I., Vadas, S. L., Crowley, G., & Makela, J. (2017). Traveling ionospheric disturbances over the united states induced by gravity waves from the 2011 Tohoku tsunami and comparison with gravity wave dissipative theory. *Journal of Geophysical Research: Space Physics*, *122*, 3430–3447. <https://doi.org/10.1002/2016JA023659>
- Bacmeister, J. T., & Schoeberl, M. R. (1989). Breakdown of vertically propagating two-dimensional gravity waves forced by orography. *Journal of the Atmospheric Sciences*, *46*, 2109–2134.
- Becker, E. (2009). Sensitivity of the upper mesosphere to the Lorenz energy cycle of the troposphere. *Journal of the Atmospheric Sciences*, *66*, 647–666. <https://doi.org/10.1175/2008JAS2735.1>
- Becker, E. (2012). Dynamical control of the middle atmosphere. *Space Science Reviews*, *168*, 283–314. <https://doi.org/10.1007/s11214-011-9841-5>
- Becker, E. (2017). Mean-flow effects of thermal tides in the mesosphere and lower thermosphere. *Journal of the Atmospheric Sciences*, *74*, 2043–2063. <https://doi.org/10.1175/JAS-D-16-0194.1>
- Becker, E., & Brune, S. (2014). Reply to "Comments on 'Indications of stratified turbulence in a mechanistic GCM'". *Journal of the Atmospheric Sciences*, *71*, 858–862. <https://doi.org/10.1175/JAS-D-13-0281.1>
- Becker, E., & Burkhardt, U. (2007). Nonlinear horizontal diffusion for GCMs. *Monthly Weather Review*, *133*, 1439–1454.

- Becker, E., & von Savigny, C. (2010). Dynamical heating of the polar summer mesopause induced by solar proton events. *Journal of Geophysical Research*, *115*, D00118. <https://doi.org/10.1029/2009JD012561>
- Becker, E., Knöpfel, R., & Lübken, F.-J. (2015). Dynamically induced hemispheric differences in the seasonal cycle of the summer polar mesopause. *Journal of Atmospheric and Solar-Terrestrial Physics*, *129*, 128–141. <https://doi.org/10.1016/j.jastp.2015.04.014>
- Beldon, C. L., & Mitchell, N. J. (2010). Gravity wave-tidal interactions in the mesosphere and lower thermosphere over Rothera, Antarctica (68°S, 68°W). *Journal of Geophysical Research*, *115*, D18101. <https://doi.org/10.1029/2009JD013617>
- Brune, S., & Becker, E. (2013). Indications of stratified turbulence in a mechanistic GCM. *Journal of the Atmospheric Sciences*, *70*, 231–247. <https://doi.org/10.1175/JAS-D-12-025.1>
- Chen, C., & Chu, X. (2017). Two-dimensional Morlet wavelet transform and its application to wave recognition methodology of automatically extracting two-dimensional wave packets from lidar observations in Antarctica. *Journal of Atmospheric and Solar-Terrestrial Physics*, *162*, 28–47. <https://doi.org/10.1016/j.jastp.2016.10.016>
- Chen, C., Chu, X., McDonald, A. J., Vadas, S. L., Yu, Z., Fong, W., & Lu, X. (2013). Inertia-gravity waves in Antarctica: A case study using simultaneous lidar and radar measurements at McMurdo/Scott Base (77.8°S, 166.7°E). *Journal of Geophysical Research: Atmospheres*, *118*, 2794–2808. <https://doi.org/10.1002/jgrd.50318>
- Chen, C., Chu, X., Zhao, J., Roberts, B. R., Yu, Z., Fong, W., et al. (2016). Lidar observations of persistent gravity waves with periods of 3–10 h in the Antarctic middle and upper atmosphere at McMurdo (77.83°S, 166.67°E). *Journal of Geophysical Research: Space Physics*, *121*, 1483–1502. <https://doi.org/10.1002/2015JA022127>
- de Wit, R. J., Janches, D., Fritts, D. C., Stockwell, R., & Coy, L. (2017). Unexpected climatological behavior of MLT gravity wave momentum flux in the lee of the Southern Andes hotspot. *Geophysical Research Letters*, *44*, 1182–1191. <https://doi.org/10.1002/2016GL072311>
- Fomichev, V. I., Ward, W. E., Beagley, S. R., McLandress, C., McConnell, J. C., McFarlane, N. A., & Shepherd, T. G. (2002). Extended Canadian Middle Atmosphere Model: Zonal-mean climatology and physical parameterizations. *Journal of Geophysical Research*, *107*(D10), 4087. <https://doi.org/10.1029/2001JD000479>
- Franke, P. M., & Robinson, W. A. (1999). Nonlinear behavior in the propagation of atmospheric gravity waves. *Journal of the Atmospheric Sciences*, *56*, 3010–3027.
- Fritts, D. C., & Alexander, M. J. (2003). Gravity wave dynamics and effects in the middle atmosphere. *Reviews of Geophysics*, *41*(1), 1003. <https://doi.org/10.1029/2001RG000106>
- Fritts, D. C., Vadas, S. L., & Yamada, Y. (2002). An estimate of strong local body forcing and gravity wave radiation based on OH airglow and meteor radar observations. *Geophysical Research Letters*, *29*(10), 1429. <https://doi.org/10.1029/2001GL013753>
- Fritts, D. C., Vadas, S. L., Wan, K., & Werne, J. A. (2006). Mean and variable forcing of the middle atmosphere by gravity waves. *Journal of Atmospheric and Solar-Terrestrial Physics*, *68*, 247–265. <https://doi.org/10.1016/j.jastp.2005.04.010>
- Garcia, R. R., Lieberman, R., Russell III, J. M., & Mlynczak, M. G. (2005). Large-scale waves in the mesosphere and lower thermosphere observed by SABER. *Journal of the Atmospheric Sciences*, *62*, 4384–4399. <https://doi.org/10.1175/JCLI-D-12-00545.1>
- Geller, M. A., Alexander, M. J., Love, P. T., Bachmeister, J., Ern, M., Hertzog, A., et al. (2013). A comparison between gravity wave momentum fluxes in observations and climate models. *Journal of Climate*, *26*, 6383–6405. <https://doi.org/10.1175/JCLI-D-12-00545.1>
- Hendricks, E. A., Doyle, J. D., Eckermann, S. D., Jiang, Q., & Reinecke, A. (2014). What is the source of the stratospheric gravity wave belt in austral winter. *Journal of the Atmospheric Sciences*, *71*, 1583–1592. <https://doi.org/10.1175/JAS-D-13-0332.1>
- Hines, C. O., & Reddy, C. A. (1967). On the propagation of atmospheric gravity waves through regions of wind shear. *Journal of Geophysical Research*, *72*, 1015–1034.
- Hong, S.-S., & Lindzen, R. S. (1976). Solar semidiurnal tide in the thermosphere. *Journal of the Atmospheric Sciences*, *33*, 135–153.
- Kinoshita, T., Murayama, Y., & Kawamura, S. (2015). Tidal modulations of mesospheric gravity wave kinetic energy observed with MF radar at Poker Flat Research Range, Alaska. *Journal of Geophysical Research: Atmospheres*, *120*, 6379–6390. <https://doi.org/10.1002/2014JD022647>
- Lindzen, R. S. (1973). Wave-mean flow interaction in the upper atmosphere. *Boundary Layer Meteorology*, *4*, 327–343.
- Lindzen, R. S. (1981). Turbulence and stress owing to gravity wave and tidal breakdown. *Journal of Geophysical Research*, *86*, 9707–9714.
- Lindzen, R. S. (1990). *Dynamics in atmospheric physics* (p. 310). Cambridge, UK: Cambridge University Press.
- Liu, H.-L., McInerney, J. M., Santos, S., Lauritzen, P. H., Taylor, M. A., & Pedatella, N. M. (2014). Gravity waves simulated by high-resolution Whole Atmosphere Community Climate Model. *Geophysical Research Letters*, *41*, 9106–9112. <https://doi.org/10.1002/2014GL062468>
- Lu, X., Chu, X., Fuller-Rowell, T., Chang, L., Fong, W., & Yu, Z. (2013). Eastward propagating planetary waves with periods of 1–5 days in the winter Antarctic stratosphere as revealed by MERRA and lidar. *Journal of Geophysical Research: Atmospheres*, *118*, 9565–9578. <https://doi.org/10.1002/jgrd.50717>
- McLlandress, C., Ward, W. E., Fomichev, V. I., Semeniuk, K., Beagley, S. R., McFarlane, N. A., & Shepherd, T. G. (2006). Large-scale dynamics of the mesosphere and lower thermosphere: An analysis using the extended Canadian Middle Atmosphere Model. *Journal of Geophysical Research*, *111*, D17111. <https://doi.org/10.1029/2005JD006776>
- Nicolls, M. J., Vadas, S. L., Aponte, N., & Sulzer, M. P. (2014). Horizontal wave parameters of daytime thermospheric gravity waves and E-region neutral winds over Puerto Rico. *Journal of Geophysical Research: Space Physics*, *119*, 576–600. <https://doi.org/10.1002/2013JA018988>
- O'Sullivan, D., & Dunkerton, T. J. (1995). Generation of inertia-gravity waves in a simulated life-cycle of baroclinic instability. *Journal of the Atmospheric Sciences*, *52*, 3695–3716.
- Plougonven, R., & Zhang, F. (2014). Internal gravity waves from atmospheric jets and fronts. *Reviews of Geophysics*, *52*, 33–76. <https://doi.org/10.1002/2012RG000419>
- Rienecker, M. M., Suarez, M. J., Gelaro, R., Todling, R., Bacmeister, J., Liu, E., et al. (2011). MERRA: NASA's modern-era retrospective analysis for research and applications. *Journal of Climate*, *24*, 3624–3648. <https://doi.org/10.1175/JCLI-D-11-00015.1>
- Sato, K., Tani, S., Watanabe, S., & Kawatani, Y. (2012). Gravity wave characteristics in the southern hemisphere revealed by a high-resolution middle-atmosphere general circulation model. *Journal of the Atmospheric Sciences*, *69*, 1378–1396. <https://doi.org/10.1175/JAS-D-11-0101.1>
- Sato, K., & Nomoto, M. (2015). Gravity-wave induced anomalous potential vorticity gradient generating planetary waves in the winter mesosphere. *Journal of the Atmospheric Sciences*, *72*, 3609–3624. <https://doi.org/10.1175/JAS-D-15-0046.1>
- Satomura, T., & Sato, K. (1999). Secondary generation of gravity waves associated with the breaking of mountain waves. *Journal of the Atmospheric Sciences*, *56*, 3847–3858.
- Shaw, T., & Becker, E. (2011). Comments on "A spectral parameterization of drag, eddy diffusion, and wave heating for a three-dimensional flow induced by breaking gravity waves". *Journal of the Atmospheric Sciences*, *68*, 2465–2469. <https://doi.org/10.1175/2011JAS3663.1>
- Simmons, A. J., & Burridge, D. M. (1981). An energy and angular momentum conserving vertical finite-difference scheme and hybrid vertical coordinates. *Monthly Weather Review*, *109*, 758–766.

- Smagorinsky, J. (1993). Some historical remarks on the use of nonlinear viscosities. In B. Galperin & St. A. Orszag (Eds.), *Large eddy simulation of complex engineering and geophysical flows* (pp. 3–36). Cambridge, UK: Cambridge University Press.
- Smith, A. K. (2012). Global dynamics of the MLT. *Surveys in Geophysics*, 33, 1177–1230. <https://doi.org/10.1007/s10712-012-9196-9>
- Smith, R. B., Nugent, A. D., Kruse, C. G., Fritts, D. C., Doyle, J. D., Eckermann, S. D., et al. (2016). Stratospheric gravity wave fluxes and scales during DEEPWAVE. *Journal of the Atmospheric Sciences*, 73, 2581–2869. <https://doi.org/10.1175/JAS-D-15-0324.1>
- Stober, G., Jacobi, C., Matthias, V., Hoffmann, P., & Gerding, M. (2012). Neutral air density variations during strong planetary wave activity in the mesopause region derived from meteor radar observations. *Journal of Atmospheric and Solar-Terrestrial Physics*, 74, 55–63. <https://doi.org/10.1016/j.jastp.2011.10.007>
- Vadas, S. L. (2007). Horizontal and vertical propagation and dissipation of gravity waves in the thermosphere from lower atmospheric and thermospheric sources. *Journal of Geophysical Research*, 112, A06305. <https://doi.org/10.1029/2006JA011845>
- Vadas, S. L., & Crowley, G. (2010). Sources of the traveling ionospheric disturbances observed by the ionospheric TIDDBIT sounder near Wallops Island on October 30, 2007. *Journal of Geophysical Research*, 115, A07324. <https://doi.org/10.1029/2009JA015053>
- Vadas, S. L., & Crowley, G. (2017). Neutral wind and density perturbations in the thermosphere created by gravity waves observed by the TIDDBIT sounder. *Journal of Geophysical Research: Space Physics*, 122, 6652–6678. <https://doi.org/10.1002/2016JA023828>
- Vadas, S. L., & Fritts, D. C. (2001). Gravity wave radiation and mean responses to local body forces in the atmosphere. *Journal of the Atmospheric Sciences*, 58, 2249–2279.
- Vadas, S. L., & Fritts, D. C. (2002). The importance of spatial variability in the generation of secondary gravity waves from local body forces. *Geophysical Research Letters*, 29(20), 1984. <https://doi.org/10.1029/2002GL015574>
- Vadas, S. L., & Liu, H.-L. (2009). Generation of large-scale gravity waves and neutral winds in the thermosphere from the dissipation of convectively generated gravity waves. *Journal of Geophysical Research*, 114, A10310. <https://doi.org/10.1029/2009JA014108>
- Vadas, S. L., & Liu, H.-L. (2013). Numerical modeling of the large-scale neutral and plasma responses to the body forces created by the dissipation of gravity waves from 6 h of deep convection in Brazil. *Journal of Geophysical Research: Space Physics*, 118, 2593–2617. <https://doi.org/10.1002/jgra.50249>
- Vadas, S. L., & Nicolls, M. J. (2009). Temporal evolution of neutral, thermospheric winds and plasma response using PFISR measurements of gravity waves. *Journal of Atmospheric and Solar-Terrestrial Physics*, 71, 740–770.
- Vadas, S. L., Fritts, D. C., & Alexander, M. J. (2003). Mechanisms for the generation of secondary waves in wave breaking regions. *Journal of the Atmospheric Sciences*, 60, 194–214. <https://doi.org/10.1029/2004JD005574>
- Watanabe, S., & Miyahara, S. (2009). Quantification of the gravity wave forcing of the migrating diurnal tide in gravity wave-resolving general circulation model. *Journal of Geophysical Research*, 114, D07110. <https://doi.org/10.1029/2008JD011218>
- Watanabe, S., Kawatani, Y., Tomikawa, Y., Miyazaki, K., Takahashi, M., & Sato, K. (2008). General aspects of a T213L256 middle atmosphere general circulation model. *Journal of Geophysical Research*, 113, D12110. <https://doi.org/10.1029/2008JD010026>
- Watanabe, S., Sato, K., & Takahashi, M. (2006). A general circulation model study of the orographic gravity waves over Antarctica excited by katabatic winds. *Journal of Geophysical Research*, 111, D18104. <https://doi.org/10.1029/2005JD006851>
- Yamashita, C., Chu, X., Liu, H.-L., Espy, P. J., Nott, G. J., & Huang, W. (2009). Stratospheric gravity wave characteristics and seasonal variations observed by lidar at the South Pole and Rothera, Antarctica. *Journal of Geophysical Research*, 114, D12101. <https://doi.org/10.1029/2008JD011472>
- Zhao, J., Chu, X., Chen, C., Lu, X., Fong, W., Yu, Z., et al. (2017). Lidar observations of stratospheric gravity waves from 2011 to 2015 at McMurdo (77.84°S, 166.69°E), Antarctica: 1. Vertical wavelengths, periods, and frequency and vertical wavenumber spectra. *Journal of Geophysical Research: Atmospheres*, 122, 5041–5062. <https://doi.org/10.1002/2016JD026368>